RESEARCH ARTICLE | APRIL 06 2026

Density ratio effects on the simulated plane turbulent mixing layer

W. A. McMullan ; J. X. Huang; S. N. Hug ; J. Mifsud ; S. J. Garrett

Physics of Fluids 38, 045122 (2026)
https://doi.org/10.1063/5.0322310

Physics of Fluids ARTICLE pubs.aip.org/aip/pof

Density ratio effects on the simulated plane turbulent mixing layer

Cite as: Phys. Fluids **38**, 045122 (2026); doi: 10.1063/5.0322310
Submitted: 12 January 2026 · Accepted: 17 March 2026 ·
Published Online: 6 April 2026

View Online Export Citation CrossMark

W. A. McMullan,[1,a)] J. X. Huang,[2] S. N. Hug,[2] J. Mifsud,[3] and S. J. Garrett[4]

AFFILIATIONS

[1]College of Engineering and Physical Sciences, Aston University, Birmingham B4 7ET, United Kingdom
[2]School of Engineering, University of Leicester, University Road, Leicester LE1 7RH, United Kingdom
[3]School of Energy, Geoscience, Infrastructure and Society, Heriot-Watt University, Edinburgh EH14 4AS, United Kingdom
[4]AIFE, Melbourne, Surrey Hills, Victoria 3127, Australia

[a)]**Author to whom correspondence should be addressed:** a.mcmullan@aston.ac.uk

ABSTRACT

We present the results from a large eddy simulation (LES) study of the plane turbulent mixing layer, at various values of density ratio, and velocity ratio, between the constituent freestreams. The inflow conditions are representative of those found in laboratory experiments with clean laminar upstream initial conditions. A low-Mach number approximation solver is used to perform the LES, and an inflow condition generator produces upstream conditions which mimic those found in laboratory experiments. The simulated mixing layers display modifications to the visual thickness growth rate as a function of density and velocity ratio that are in excellent agreement with experimental observations. The mean flow statistics are biased toward the low-density stream, and the magnitude of the turbulent statistics display a functional dependence on the velocity ratio, for non-uniform density flows. The "Brown–Roshko" structure is observed for all values of density ratio. It is shown that the mean structure spacing is a function of both density ratio and velocity ratio, with the mean structure spacing scaling universally as approximately 1.5 times the local visual thickness. The evolution of the streamwise structure is functionally the same for all values of density ratio, and the streamwise structures lose their coherence downstream of a non-dimensional pairing parameter greater than 16, corresponding to the third generation of interactions between primary spanwise structures. The influence of baroclinic torque on the variable density flow is examined. The results of the study are discussed in the context of the archival literature.

I. INTRODUCTION

The variable density turbulent shear layer can be found in a wide range of mixing and combustion applications. In its simplest configuration, the variable density mixing layer is formed through the merging of two planar parallel streams of fluid of differing velocity and density, downstream of a splitter plate. Canonical experimental studies of the variable density plane turbulent mixing layer have typically originated from laminar upstream conditions, with low level background fluctuations, which are normally referred to as "clean" initial conditions. The pioneering work of Brown and Roshko highlighted the influence of the density ratio on the growth rate of the layer, and the study also revealed the presence of large-scale, spanwise-orientated turbulent vortex structures (hereinafter referred to as the "Brown–Roshko structure"),[1] which persisted across all studied values of the density ratio, and to Reynolds numbers that are considered far in excess of that required for the flow to be considered representative of fully-developed turbulence.[2] Following the discovery of the Brown–Roshko structure, experimental research probed their dynamical significance for a range of Reynolds numbers, Schmidt numbers, and flows undergoing exothermic reaction.[3–10] For the isothermal variable density flow, the research by Brown and Roshko suggested an influence of the density ratio on the spacing of the turbulent spanwise vortex structures, but there has been no subsequent experimental measurements to quantify this dependency for a wide range of values of the density ratio, and the velocity ratio. Based on the limited experimental evidence available,[1,11] models describing the growth and entrainment of the turbulent mixing layer have been developed.[12,13]

Experimental research has highlighted the presence of a "streaky" structure in the mixing layer, orientated parallel to the streamwise axis,[11] which forms an integral part of the Brown–Roshko structure. The streaks were found to be a streamwise vortex structure that, in a mean sense, was statistically stationary.[14–17] The streamwise vortices in

the mixing layer originated from the presence of low-level streamwise vorticity in the upstream laminar boundary layer,[15] embedded within what would nominally be considered a two-dimensional Blasius boundary layer. Small spanwise non-uniformities in the upstream flow, arising from geometric defects in the smoothing screens, nicks in the splitter plate, or other small imperfections in the upstream flow conditioning, were responsible for the development of the residual streamwise vorticity.[15–18] Measurements have shown that the streamwise vortex structure evolves with downstream distance in the layer,[15,19] and evidence suggests that the ratio of the spanwise wavelength of the streamwise structure to the local mixing layer vorticity thickness attains an asymptotic value of approximately unity.[14,15,17] This behavior, however, has not been fully confirmed for a wide range of the density ratio.

A variable density mixing layer will be subjected to baroclinic torque, owing to the misalignment of the density gradient and the pressure gradient. Detailed statistical information on the nature of the large-scale structures in mixing layers, and of the effects of baroclinic torque on the flow, are difficult to ascertain experimentally owing to the short run times offered by the use of bottled gas as the supply of low-density fluid.[1,6,14] Direct numerical simulation (DNS) and large eddy simulation (LES) offer the potential to study the influence of the density ratio on the mixing layer in fine detail; the most common form of variable density mixing layer simulation reported in the literature has been of the temporally evolving form, owing to the relatively low computational expense of the configuration, and the removal of the need to specify time-dependent inflow conditions.[20–23] Extensive numerical simulation studies have been reported on the spatially evolving compressible mixing layer, where the reduction of the layer growth rate as a function of convective Mach number remains an active area of research interest.[24–30] Spatially evolving simulations of the variable mixing layer in the incompressible regime have been typically confined to a two-dimensional box,[31] where the layer grows through amalgamative interactions between the unsteady laminar Kelvin–Helmholtz (K–H) vortices, and a streamwise structure is necessarily absent from the flow. It was observed that the baroclinic torque-created vorticity of opposite signs across each spanwise vortex structure was then linked to the alteration of the eddy speed through considering its contribution as that of a dipole of vortices of opposite signs spanning the vortex structure. Recent numerical research has shown that, in order for three-dimensional LES to accurately capture both the stationary streamwise-orientated vortex structures, and the spanwise-orientated vortex structures which comprise the Brown–Roshko structure, it is essential to impose an inflow condition on the simulation which recreates the spanwise non-uniformities found in the experimental upstream laminar flow conditions.[32–35] Such simulations of the laboratory mixing layer are distinct from those which use idealized inflow conditions perturbed by Gaussian white noise disturbances, where a stationary streamwise structure is absent from the flow.[32,36–38] The majority of published research on simulations of the laboratory mixing layer have been performed at uniform density conditions, but a more recent three-dimensional large eddy simulation (LES) study has demonstrated the potential of LES to successfully capture the dynamics of the laboratory variable density mixing layer, when appropriate inflow conditions are imposed.[39] The effects of both the density ratio and the velocity ratio on the statistical properties of the spanwise structures, and the streamwise structures, have yet to be fully quantified by numerical simulation. In addition, information on the effect of baroclinic torque on the stationary streamwise structure is lacking.

This paper aims to quantify the effect of the density ratio, and of the velocity ratio, on the laboratory mixing layer, with a particular emphasis on the large-scale structures present in the flow. A well-established LES methodology will be used to simulate variable density mixing layers in an incompressible formulation, through the low Mach number approximation. The mixing layers simulated here cover a range of the density ratio, $s = \rho_2/\rho_1$, from 0.138 to 7.23, and a range of the velocity ratio parameter, $\lambda = (U_1 - U_2)/(U_1 + U_2)$, from 0.39 to 0.66. The transition to turbulence in the simulated layer is typically completed by a local Reynolds number, based on the local visual thickness and the velocity difference across the layer, $\mathrm{Re}_\delta = (U_1 - U_2)\delta_{viz}/\nu$ of approximately 10 000,[39] as is expected for free shear flows.[2] The maximum local Reynolds number attained in the simulations is approximately 315 000. For the current flow conditions, the maximum Richardson number, $\mathrm{Ri} \approx \Delta\rho g \delta_{viz}/\rho_0 (U_1 - U_2)^2 \approx 0.004$, an order of magnitude lower than the threshold postulated for buoyancy effects to become important in the mixing layer.[40]

The paper is organized as follows. The numerical methods used in the research are outlined in Sec. II. The setup of the simulations is outlined in Sec. III. The computed flow statistics of the simulations are presented in Sec. IV. The properties of the large-scale spanwise turbulent vortex structures, and the streamwise vortex structure, are presented in Sec. V. The effect of baroclinic torque on the vortex structures is discussed in Sec. VI. The results are discussed in the context of the literature in Sec. VII, and concluding remarks are drawn in Sec. VIII. An overview of the influence of variable viscosity on the variable density mixing layer prediction is provided in the Appendix.

II. NUMERICAL METHODS

The research code used here takes advantage of the low-Mach number approximation to simulate variable density flows in an incompressible formulation. The pressure and density fields are therefore decoupled, removing acoustic effects from the flow. A finite volume method is used to solve the governing equations, with a staggered-cell arrangement for the primitive variables.

The current research focuses on the large eddy simulation of incompressible, isothermal, low-speed variable density mixing layers, where strong density fluctuations can occur. These fluctuations are treated through the introduction of Favre-filtered quantities, given by

$$\tilde{\phi}_i = \frac{\overline{\rho\phi_i}}{\overline{\rho}}, \tag{1}$$

where a quantity $\overline{\phi_i}$ denotes a spatially filtered variable. It is assumed that Fick's Law of diffusion is valid, and that the Lewis number is unity. Body forces, including gravity, are also ignored in the current research. The transport of the constituent gases at isothermal, non-reacting conditions is modeled through the solution of the mixture fraction transport equation. Given the above assumptions, and applying an implicit top-hat filter to the governing equations, leads to the Favre-filtered low-Mach number equations of continuity, momentum, and mixture fraction transport. These are written as

$$\frac{\partial\overline{\rho}}{\partial t} + \frac{\partial\overline{\rho}\tilde{u}_i}{\partial x_i} = 0, \tag{2}$$

$$\frac{\partial \overline{\rho}\tilde{u}_i}{\partial t} + \frac{\partial \overline{\rho}\tilde{u}_i\tilde{u}_j}{\partial x_j} = -\frac{\partial \overline{p}}{\partial x_i} + \frac{\partial \tau_{ij}}{\partial x_j} - \frac{\partial T_{ij}}{\partial x_j}, \tag{3}$$

$$\frac{\partial \overline{\rho}\tilde{\xi}}{\partial t} + \frac{\partial \overline{\rho}\tilde{u}_i\tilde{\xi}}{\partial x_i} = \frac{\partial J_i}{\partial x_i} - \frac{\partial M_i}{\partial x_i}, \tag{4}$$

where $\overline{\rho}$ is the density, $\tilde{u}_i$ is the velocity, $\tilde{\xi}$ is the mixture fraction, $\overline{p}$ is the pressure, and τ_{ij} is the viscous stress tensor. For a Newtonian fluid obeying Fick's law of diffusion, the mass flux is given by $J_i = \gamma(\partial\tilde{\xi}/\partial x_i)$, where $\gamma = \overline{\rho}\Gamma$ denotes the mass diffusivity coefficient. The Favre filtering operation introduces terms into the governing equations which must be modeled to close the system. The subgrid stress and mass flux tensors are given by $T_{ij} = \overline{\rho}(\widetilde{u_i u_j} - \tilde{u}_i\tilde{u}_j)$ and $M_i = \overline{\rho}(\widetilde{u_i\xi} - \tilde{u}_i\tilde{\xi})$, respectively.

A subgrid-scale model is used to close the governing equations. The wall-adapting local eddy-viscosity (WALE) model[41] is used here to model the subgrid stresses. The subgrid viscosity is computed through

$$\mu_{sgs} = \overline{\rho}(C_w\overline{\Delta})^2 \frac{(S^d_{ij}S^d_{ij})^{3/2}}{(\tilde{S}_{ij}\tilde{S}_{ij})^{5/2} + (S^d_{ij}S^d_{ij})^{5/4}}, \tag{5}$$

where $\tilde{S}_{ij} = \frac{1}{2}(\partial\tilde{u}_i/\partial x_j + \partial\tilde{u}_j/\partial x_i)$, $S^d_{ij} = \frac{1}{2}(\tilde{g}^2_{ij} + \tilde{g}^2_{ji}) - \frac{1}{3}\delta_{ij}\tilde{g}^2_{kk}$, $\tilde{g}^2_{ij} = \tilde{g}_{ik}\tilde{g}_{kj}$, $\tilde{g}_{ij} = \partial\tilde{u}_i/\partial x_j$, and δ_{ij} is the Kronecker Delta. The wall-adapting local eddy-viscosity (WALE) model captures the correct near-wall behavior of the subgrid viscosity and computes zero subgrid viscosity in regions of laminar flow. These features make the model attractive for shear layer simulations where the flow originates from laminar upstream conditions, and it has been used extensively for simulations of plane turbulent mixing layers.[32,35,36,42] In this formulation, the WALE model does not explicitly account for the effects of subgrid-scale baroclinic torque on the flow.

The mixture fraction transport equation is closed using the gradient-diffusion model, given by

$$M_i = -\frac{\mu_{sgs}}{\mathrm{Sc}_t}\left(\frac{\partial\tilde{\xi}}{\partial x_i}\right), \tag{6}$$

and the subgrid-scale Schmidt number is assumed constant, with $\mathrm{Sc}_t = 0.7$. The density field is related to the mixture fraction through the relation

$$\frac{1}{\overline{\rho}} = \frac{\tilde{\xi}}{\rho_1} + \frac{1-\tilde{\xi}}{\rho_2}, \tag{7}$$

where ρ_1 and ρ_2 are the freestream densities of the high- and low-speed streams, respectively.

A second-order accurate central differencing scheme is employed for the solution of the momentum equation. A third-order accurate total variation diminishing (TVD) scheme is used for the convective and diffusive terms in the scalar transport equation. The pressure field is computed using a multi-grid method. The outflow condition is of standard convective form and has been shown to be passive.[32,43,44] The second-order accurate Adams–Bashforth method is used to advance the governing equations forward in time.

The recycling and rescaling procedure of Xiao *et al.*[45] provides the inflow conditions for the current study. Virtual domains are created upstream of the main simulation domain, in which the flow at a sampling plane is recycled onto the inlet plane of the virtual domain, and the flow within the virtual domain is periodically rescaled to a target set of statistics. The flow passes from the virtual domains directly into the main simulation domain, allowing the inflow generation and the main simulation to run concurrently. This method has been used in the literature to provide excellent predictions of turbulent shear flow in a wide variety of configurations.[35,42,45–48] A complete description of its implementation can be found elsewhere.[35]

III. SIMULATION SETUP

The short run times enforced through the use of bottled gas in experiments of incompressible variable density mixing layer experiments means that the initial conditions of such flows at the trailing edge of the splitter plate are poorly-documented,[1,6,14,49] with insufficient information available to permit exact numerical replication by LES. For the present research, it was consequently decided that a uniform density experiment would provide the reference experimental data, with the density ratio, s, systematically varied in the simulations. Cases 1–3 have the low-density fluid in the low-speed stream, cases 4–6 are uniform density, and cases 7–9 have the low-density fluid in the high-speed stream. For a given value of the density ratio, simulations are performed at velocity ratio parameter values of $\lambda = 0.39$, 0.52, and 0.66. The bulk flow properties of the simulations are detailed in Table I. A constant value of the dynamic viscosity of both constituent gases is assumed, with its value being that of air at 293 K.

TABLE I. Bulk flow properties of the simulations performed in the research.

Case	U_1 (m s^{-1})	U_2 (m s^{-1})	θ_1 (mm)	θ_2 (mm)	s	λ	Re_δ (max)
1	25.6	11.2	0.46	0.86	0.138	0.39	82 500
2	25.6	8.0	0.46	0.86	0.138	0.52	127 800
3	25.6	5.2	0.46	0.86	0.138	0.66	178 800
4	25.6	11.2	0.46	0.86	1.0	0.39	97 150
5	25.6	8.0	0.46	0.86	1.0	0.52	158 300
6	25.6	5.2	0.46	0.86	1.0	0.66	233 000
7	25.6	11.2	0.46	0.86	7.23	0.39	118 000
8	25.6	8.0	0.46	0.86	7.23	0.52	208 000
9	25.6	5.2	0.46	0.86	7.23	0.66	315 000

The computational domain and mesh resolution for current study match that of previous mixing layer simulations.[33–35,39] The domain extends $1650\times 1326 \times 392\theta_i$ in the streamwise, vertical, and spanwise directions respectively, with the initial momentum thickness of the mixing layer, θ_i, equivalent to the high-speed side boundary layer momentum thickness at the splitter plate trailing edge, θ_1. The computational domain for the mixing layer is discretized by $768 \times 256 \times 256$ cells and has its origin at the trailing edge of the splitter plate (i.e., $x/\theta_i = 0, y/\theta_i = 0$). In the reference experiment, the splitter plate trailing edge had a finite thickness of 0.5 mm. In the current study, the splitter plate is modeled as a knife edge of negligible thickness. This choice is justified through the experimental findings of Dziomba and Fiedler, who reported that the trailing edge thickness had no impact on the mixing layer evolution if its thickness what less than 50% of the total momentum thickness of the upstream boundary layers.[50] The present conditions satisfy this criterion. In order to capture the initial development of the mixing layer, the grid is refined in the vicinity of the splitter plate, with minimum grid spacings of $\Delta x_{\min} = 0.46\theta_i$, $\Delta y_{\min} = 0.086\theta_i$. The first 50 cells in the streamwise direction have a constant grid spacing, downstream of which an expansion factor of 1.003 stretches the grid. The first three cells from the splitter plate in the vertical direction have a constant spacing, beyond which an expansion factor of 1.047 is applied. A total of 30 cells resolved the high-speed side boundary layer. The spanwise grid spacing is held constant at $z/\theta_i = 1.54\theta_i$. The Kolmogorov microscale is a standard measure of the smallest scale of turbulence in a fluid flow. The readers of this article will understand its meaning, and that the grid resolution is a factor larger than this microscale measure.

The inflow conditions are generated in virtual domains which reside upstream of the main mixing layer domain. The domains have an extent of $112 \times 663 \times 392\theta_i$ and are discretized into $256 \times 128 \times 256$ cells. The grid resolution in the virtual domains matches that of the initial region of the mixing layer domain.

For each simulation outlined in Table I, the inflow conditions for both boundary layers are shown in Fig. 1. The angled brackets, $\langle\,\rangle$, denote a spanwise-averaged quantity. In the reference experiment, the high-speed side boundary layer was close to Blasius form. Measurements of the streamwise root mean squared (rms) fluctuations, u''/U_1, were recorded in the experiment, but these were subject to a 1% measurement error owing to the data recording methodology. No measurements were recorded for the vertical rms fluctuations, v''/U_1, and the spanwise rms fluctuations, w''/U_1. Previous simulations of uniform density mixing layers have shown that the current inflow conditions lead to small spanwise non-uniformities in the laminar boundary layers. The non-uniformities are caused by the presence of streaks in the boundary layer, which are indicative of Klebanoff modes. Similar weak vortex structures have also been observed in LES of the variable density mixing layer,[39] and they are also present in the current simulations for all values of s and λ. For all simulations, the deviation of the mean streamwise velocity from its spanwise-average value, evaluated through $(U - \langle U\rangle)/U_1$, is less than 0.5% at the trailing edge of the splitter plate, and the deviation of the rms streamwise fluctuation from its spanwise-averaged value, $(u'' - \langle u''\rangle)/U_1$ is less than 0.08%. A power spectral density (PSD) plot of the streamwise velocity fluctuations, shown in Fig. 1(c), shows that there is no particular dominant frequency, and hence the inflow condition does not artificially force the mixing layer. The inflow conditions can therefore be

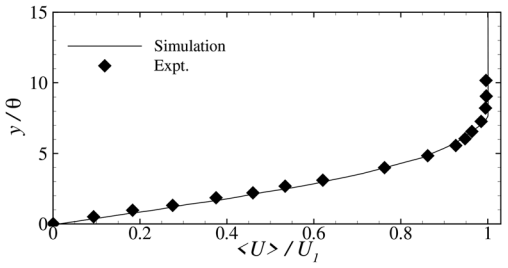

(a)Mean streamwise velocity profile.

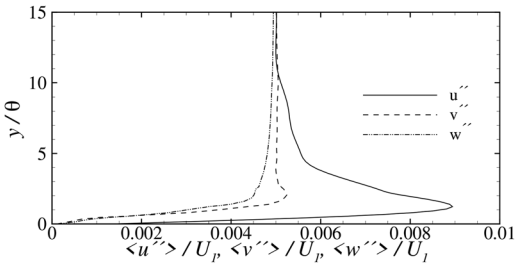

(b)Root mean squared velocity fluctuation profiles.

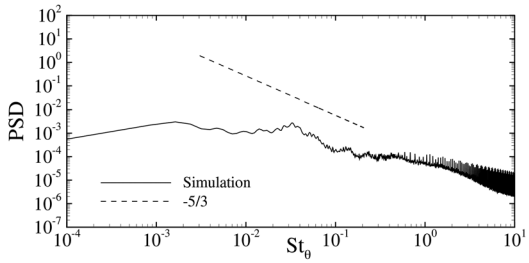

(c)Power spectral density of streamwise velocity fluctuations.

FIG. 1. Inflow conditions used in the simulations.

considered as nominally two-dimensional. The flow conditions outlined in Fig. 1 should be considered as representative of "clean" initial conditions found in laboratory experiments of mixing layers originating from upstream laminar boundary layers, for all values of s and λ considered here.

In the virtual domains, the splitter plate is modeled with a no-slip boundary condition. The flow passes from the virtual domains directly into the mixing layer domain, removing the need to store auxiliary inflow data. The upper and lower boundaries of the simulation are modeled as slip walls, and the outflow condition of standard advective form. The spanwise boundaries are periodic, with the domain sufficiently wide to permit the natural development of the streamwise vortex structure.[33,35,51] The mixture fraction is assigned a value of unity in the high-speed stream, and zero in the low-speed stream, with the density of each stream set according to the parameters outlined in Table I. Zero-gradient conditions are applied to the mixture fraction field on the upper and lower boundaries, and on the outflow boundary. The WALE subgrid scale model is used for all simulations, with its coefficient set to $C_w = 0.56$. The subgrid Schmidt number is set to $\mathrm{Sc}_t = 0.7$. Simulations 1–3 have a non-dimensional time step of $U_1 \Delta t/\theta_i = 0.0223$, and simulations 4–9 have a non-dimensional time step of $U_1 \Delta t/\theta_i = 0.0334$. The choice of time step ensures that the CFL number is maintained below 0.3 throughout each simulation. Once a statistically stationary state has been established, statistical samples are accumulated over a period of 20 convective flow-through periods. A convective flow through period is the time required for a fluid parcel to traverse the streamwise extent of the computational domain at the convection velocity, U_c, which for a variable density mixing layer is defined as

$$U_c = \frac{U_1 + U_2}{2}(1 + \Lambda\lambda), \tag{8}$$

where the density ratio parameter Λ is defined as

$$\Lambda = \frac{\sqrt{\rho_1} - \sqrt{\rho_2}}{\sqrt{\rho_1} + \sqrt{\rho_2}}. \tag{9}$$

Each simulation is performed for a total of 350 h over 192 AMD EPYC4 cores.

Owing to the presence of a statistically stationary streamwise structure in mixing layers which originate from clean laminar upstream conditions, statistical quantities are averaged in the spanwise direction where appropriate. It has been shown that spanwise averaging produces more representative flow statistics, when a stationary streamwise structure is present in the mixing layer.[15,32,35,52]

Extensive validation of the numerical methodology outlined above has been published elsewhere. In previous studies, the influence of the mesh resolution,[39] subgrid-scale model,[35,39] inflow condition type,[32,39] spanwise domain extent,[33,35,51] and imposed spanwise boundary conditions[35] have been rigorously assessed, and it has been shown that the current simulation setup produces accurate flow statistics. In this article, therefore, the focus is on the salient flow physics in the variable-density plane turbulent mixing layer. Justification for the use of a constant dynamic viscosity is provided in the Appendix.

IV. FLOW STATISTICS

Given the wide range of both the density ratio and of the velocity ratio parameter studied here, the normalization of the flow statistics must be carefully considered to account for their effects on the flow. Where appropriate, downstream distances may be normalized by the initial momentum thickness, θ_i, or through the pairing parameter, P_x. In its variable density form,[6] the pairing parameter is given by

$$P_x = \frac{0.017(U_1 - U_2)x}{U_c \theta_1}, \tag{10}$$

which reduces to the conventional relationship $P_x = \lambda x/30\theta_i$ for a uniform density flow.[16] Vertical distances are normalized by either θ_i, or the local vorticity thickness, δ_ω, defined as

$$\delta_\omega = \frac{U_1 - U_2}{\partial\langle U\rangle/\partial y|_{\max}}, \tag{11}$$

where $\partial\langle U\rangle/\partial y|_{\max}$ is the spanwise-averaged maximum local velocity gradient. Spanwise distances are normalized by θ_i.

The thickness of the mixing layer is typically measured through three distinct quantities, namely the momentum thickness, θ, the vorticity thickness, δ_ω, and the visual thickness, δ_{viz}. The momentum thickness provides a measure of the integral thickness of the mixing layer, defined here as

$$\theta = \frac{1}{\rho_1 \Delta U^2}\int_{-\infty}^{\infty} \langle\overline{\rho}\rangle(U_1 - \langle U\rangle)(\langle U\rangle - U_2)dy, \tag{12}$$

where $\Delta U = U_1 - U_2$ is the velocity difference across the layer. The momentum thickness for each simulation is shown in Fig. 2. Excellent agreement is obtained between the experimental data obtained at $\lambda = 0.66$, and the corresponding case 6. For a given density ratio, the momentum thickness growth rate increases with increasing λ, and for a given value of λ, the momentum thickness growth rate increases as a function of density ratio. Each momentum thickness distribution contains an extended region with a linear gradient, indicating self-similar growth of the layer. The distance required to achieve similarity of the momentum thickness is $x/\theta_i \approx 450$ for the $s = 0.138$, and $s = 1$ simulations (cases 1–6). The $s = 7.23$ calculations show a variation in the distance required to achieve self-similar growth as a function of λ. In case 7, the self-similar growth is achieved at $x/\theta_i \approx 800$, while in case 8 the value drops to $x/\theta_i \approx 600$, and in case 9 the distance decreases further to $x/\theta_i \approx 500$. The results obtained here are in good agreement with other simulations of the spatially developing variable density mixing layer.[39]

Plots of the vorticity thickness for each simulation grouped by density ratio are shown in Fig. 3. Each simulation demonstrates a

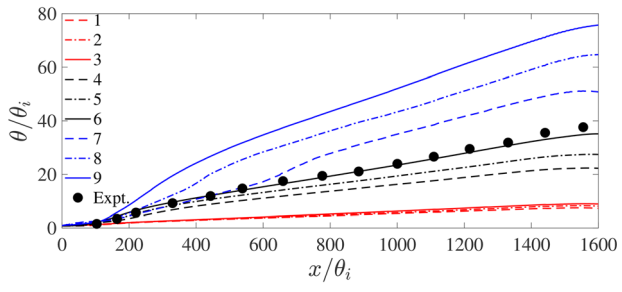

FIG. 2. Momentum thickness variation of cases 1–9. Symbols correspond to experimental data of Browand and Latigo,[53] where $s = 1$, $\lambda = 0.66$.

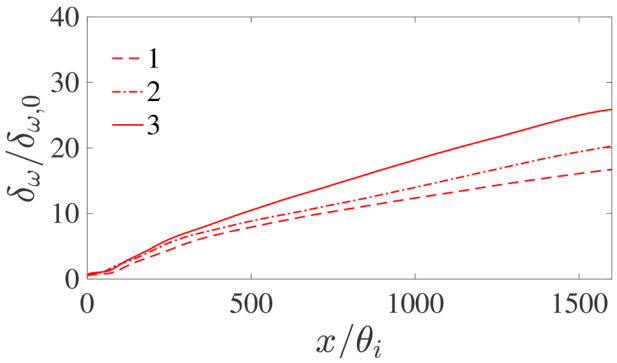

(a) $s = 0.138$.

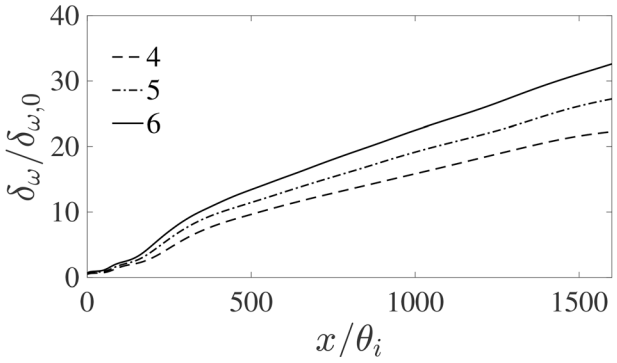

(b) $s = 1$.

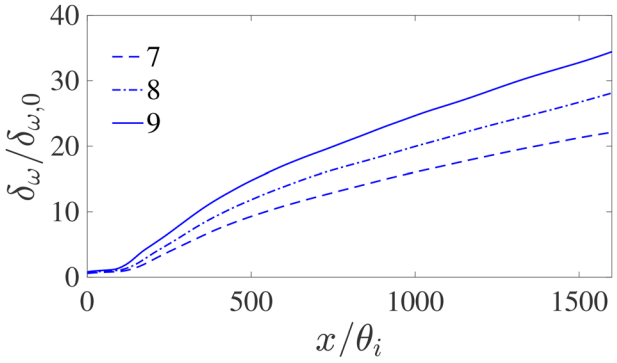

(c) $s = 7.23$.

FIG. 3. Vorticity thickness distributions of the simulations.

linear slope in the vorticity thickness curve, and the downstream distance to which similarity of the vorticity thickness is attained closely matches that observed in the momentum thickness plots of Fig. 2. For a given value of the density ratio, the vorticity thickness growth rate increases as a function of λ, in agreement with experimental data.[1,54]

The visual thickness of the mixing layer is computed by overlaying several flow visualization images of the spanwise-averaged high-speed side molar concentration, $\langle\zeta\rangle$, and tracing a wedge of the 1% thickness, i.e., the average locus of the $\langle\zeta\rangle = 0.01$, 0.99 concentration lines. The vertical distance between the wedge corresponds to the visual thickness of the layer. Tracing the 1% thickness lines back to their intersection yields the streamwise position of the virtual origin of the layer, x_0. Figure 4 plots the normalized visual thickness growth rates of all current simulations, along with available experimental data.[1] It is evident that the growth rate of the mixing layer is a function of both s, and λ. There is a favorable comparison between the predicted growth rates, and those obtained by Brown and Roshko,[1] for the range of both s and λ considered here. The lines on Fig. 4 are obtained from the relationship

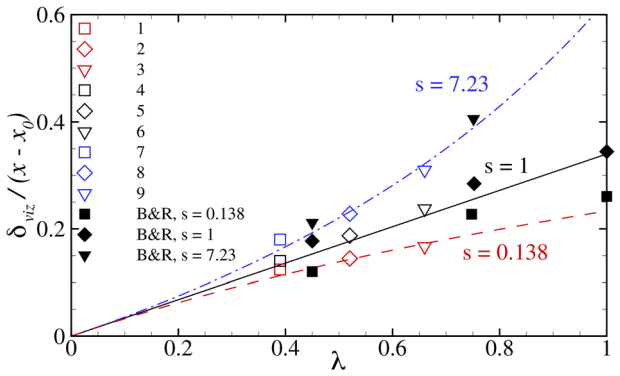

FIG. 4. Visual thickness growth rate variation of the simulations. Lines correspond to the predictions of Eq. (13), with $k_v = 0.36$. Filled symbols correspond to experimental data of Brown and Roshko.[1]

$$\delta'_{viz} = \frac{\delta_{viz}}{x - x_0} = \frac{k_v \lambda}{1 + \Lambda\lambda}. \tag{13}$$

For the present simulations, the growth rate constant has a value of $k_v \approx 0.36$, which is well within the bounds reported experimentally.[1,54] The data obtained from the current simulations are also in good agreement with the predictions of a growth and entrainment model developed on the basis of the Brown and Roshko experiments.[12]

The normalized mean streamwise velocity profiles, extracted from a downstream distance of $x/\theta_i = 1000$, are shown in Fig. 5

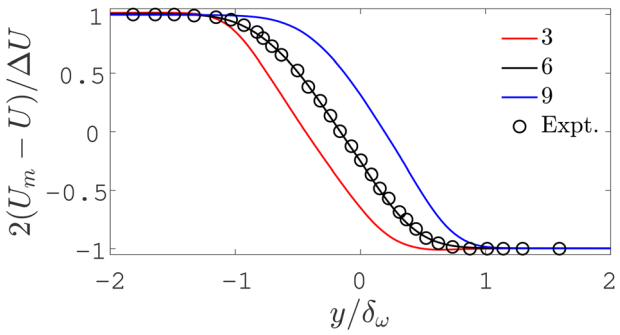

FIG. 5. Mean streamwise velocity profiles, extracted from a downstream distance of $x/\theta_i = 1000$. Experimental data correspond to flow conditions of $s = 1$, $\lambda = 0.66$.[53]

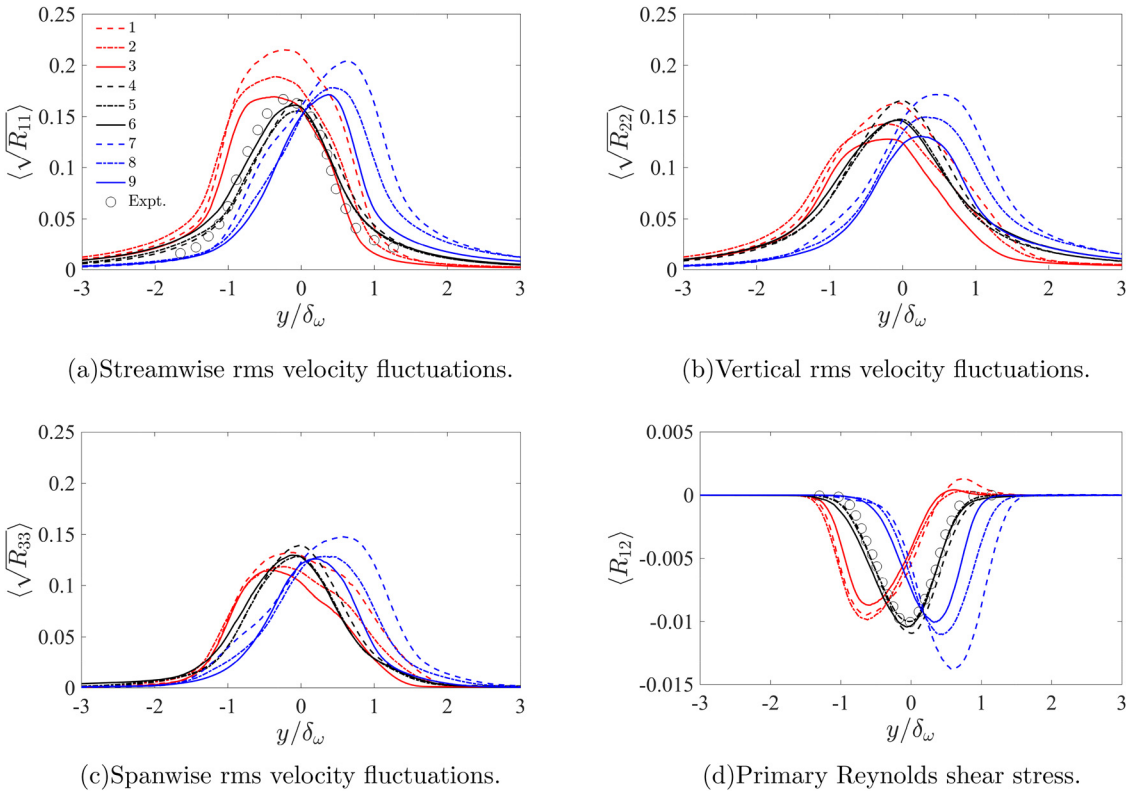

(a)Streamwise rms velocity fluctuations.

(b)Vertical rms velocity fluctuations.

(c)Spanwise rms velocity fluctuations.

(d)Primary Reynolds shear stress.

FIG. 6. Turbulence statistics extracted from the simulations at $x/\theta_i = 1000$. Experimental data in (d) recorded at uniform density conditions and at $\lambda = 0.82$.[53]

for cases 3, 6, and 9 ($\lambda = 0.66$). The normalizing quantity $U_m = 0.5(U_1 + U_2)$. All three simulations shown in Fig. 5 have obtained self-similarity at the measurement location. Plotted on the graph is the reference experimental data ($s = 1, \lambda = 0.66$). Excellent agreement is obtained between the uniform density case 6 and the experimental data. It is apparent that the effect of density ratio on the mean streamwise velocity field is to shift the profile toward the low-density stream, i.e., for case 3 ($s = 0.138$) the velocity profile is shifted toward the low speed stream, and for case 9 ($s = 7.23$), the profile is shifted toward the high-speed stream. The shifting has been observed in simulation studies of the temporal mixing layer,[21,23] and in laboratory experiments.[1] Figure 6 shows turbulence statistics extracted from all simulations at $x/\theta_i = 1000$. Favre averaging is performed on the turbulence statistics, such that the turbulent stresses are obtained from

$$R_{ij} = \frac{\overline{\rho u_i'' u_j''}}{\overline{\rho}\Delta U^2}. \tag{14}$$

The streamwise rms velocity fluctuation is shown in Fig. 6. The uniform density simulations yield good agreement with the reference experimental data, for all values of λ. For the non-uniform density simulations, the profile is shifted toward the low-density stream—a feature also observed in temporal simulations of the variable density mixing layer.[20,21,23] It is also apparent in the $s = 0.138$, 7.23 simulations that the peak magnitude of $\sqrt{R_{11}}$ decreases as a function of increasing λ. Similar trends are observed for the vertical rms velocity fluctuations, $\sqrt{R_{22}}$, and the spanwise rms velocity fluctuations, $\sqrt{R_{33}}$. The primary Reynolds shear stress, R_{12}, is plotted with experimental data obtained at uniform density conditions at a velocity ratio parameter of $\lambda = 0.82$. The primary shear stress is well-predicted by the uniform density simulations, and the profiles are again shifted toward the low-density stream in the variable density cases. A region of positive shear stress is observed toward the high-speed side of cases 1—3 ($s = 0.138$), which may be considered as a consequence of the baroclinic torque imparted on the flow by the density difference across it. This is explored further in Sec. VI.

Profiles of the spanwise-averaged mean high-speed stream concentration, $\langle\zeta\rangle$, recorded at $x/\theta_i = 1000$, are shown for all simulations in Fig. 7, grouped by density ratio. Comparable data from the experiments of Brown and Roshko,[1] and Konrad,[11] have been converted from mean density into high-speed stream molar concentration, and the vertical co-ordinate has been normalized into y/δ_{viz} based on the 1% thickness of the layer. For each value of the density ratio, there is generally good agreement between the simulations and the experimental data. It is interesting to note that, for $s = 0.138$, simulation 1 shows some discrepancy with the experiment, which is likely caused by the persistence of a strong streamwise structure at the measurement station, as will be discussed below.

Power spectral density (PSD) plots of the normalized high-speed side mole fraction fluctuations, recorded along the mixing layer centerline at $x/\theta_i = 326$ from cases 1, 4, and 7, are shown in Fig. 8. The frequency is normalized into the Strouhal number, given by

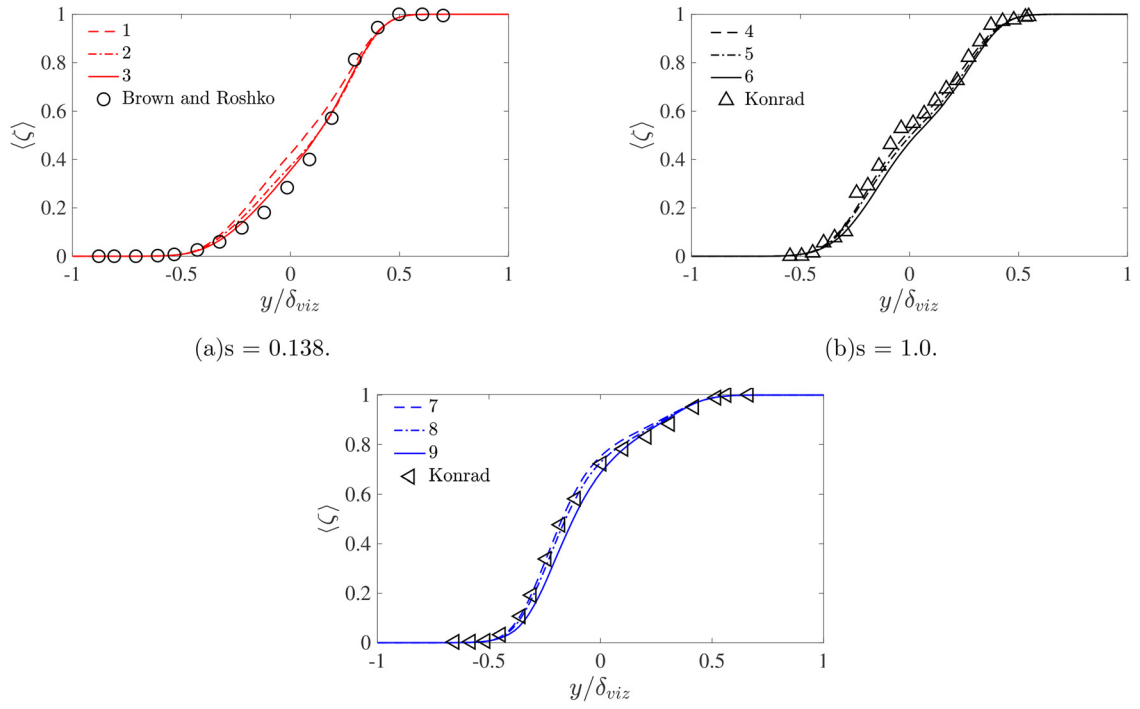

FIG. 7. Mean high-speed stream concentration profiles extracted from the simulations at $x/\theta_i = 1000$. Experimental data in (a) obtained from Brown and Rsohko,[1] and experimental data in (b) and (c) obtained from Konrad.[11] Experimental data normalized into y/δ_{viz} based on the 1% thickness of the layer.

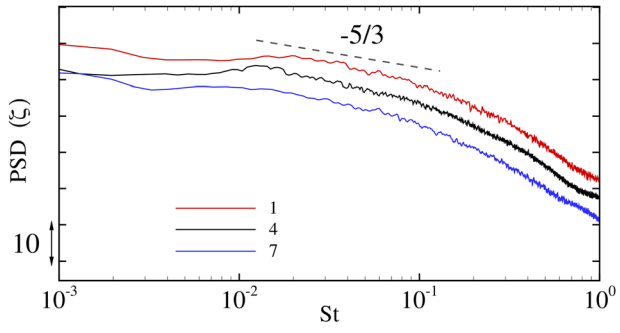

FIG. 8. Power spectral density plots of the normalized high-speed side molar concentration fluctuations. Spectra recorded at mid-span of the domain, along the plane of the mixing layer centerline.

$\mathrm{St} = f\theta_i/(U_1 - U_2)$. All plots display evidence of a $-5/3$ roll–off, which indicates that the flow is fully turbulent.

The presented flow statistics demonstrate that the uniform density flow is accurately predicted by LES, in close agreement with previous studies.[32,35] It is also shown that the effect of the density ratio on the predicted flow statistics are adequately captured, with the variations in the predicted flow statistics which arise from changes in the density ratio following those observed in other experimental, and numerical, studies of the variable density mixing layer.[1,20,21,23] It is evident that the simulated mixing layers presented here, over the range of density ratios and velocity ratios considered, are close numerical approximations of the laboratory scale mixing layer.

V. LARGE-SCALE STRUCTURES

Figure 9 shows instantaneous visualizations of the flow in cases 3 and 9. The visualizations display an isosurface of the high-speed side molar concentration, $\zeta = 0.99$, with the contour map showing the high-speed side molar concentration within the layer at the near spanwise end of the computational domain. For both cases, the initial vortex sheet rolls up into discrete K–H vortices, with pairing interactions between the spanwise vortices occurring as the flow proceeds downstream. At some downstream position, an interaction between the K–H vortices triggers the transition to turbulence. For the current conditions, this process is completed by $P_x \approx 8$, corresponding to the second generation of interactions between the vortices. Beyond the transition to turbulence, large-scale, spanwise-orientated turbulent vortex structures occupy the local visual thickness of the layer. For both images in Fig. 9, the isosurface shows a clear regular undulation across the span once the flow rolls up into discrete vortices, indicating the presence of an organized streamwise structure. For case 3, it is straightforward to trace the undulations across the span of the large-scale spanwise structures, with clear regular undulations in the isosurface present at the far downstream end of the computational domain. For case 9, however, the undulations in the isosurface become more irregular on the spanwise structures toward the downstream end of the domain.

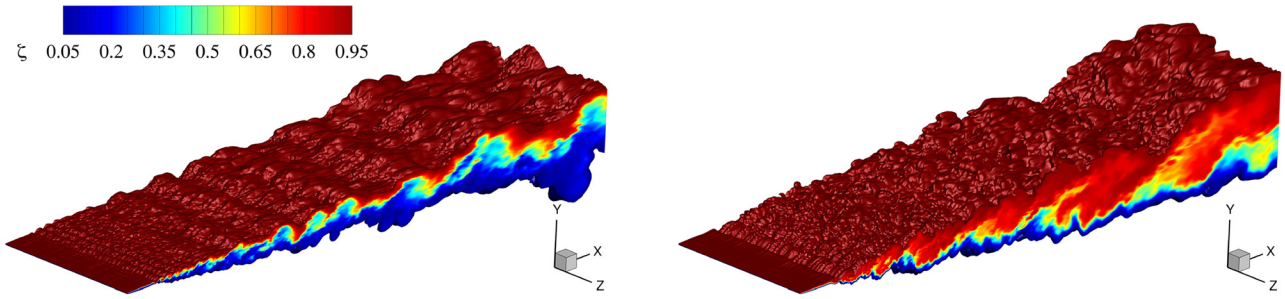

(a)Case 3, $\lambda = 0.66$, $s = 0.138$. (b)Case 9, $\lambda = 0.66$, $s = 7.23$.

FIG. 9. Visualizations of the high-speed stream molar concentration from two selected simulations. The isosurface corresponds to a value of $\zeta = 0.99$, and the interior of the layer is visualized through high-speed stream molar concentrations in the range $0.01 \leq \zeta \leq 0.99$.

To visualize the flow in a manner analogous to the optical techniques used in experiments, numerical schlieren images are produced from the divergence of the density field and scaled according to the method of Hadjadj and Kudryavtsev.[55] The images are then averaged along the axis of interrogation, to mimic the averaging process inherent in schlieren imagery. Numerical schlieren images of the instantaneous flow field in cases 3 and 9 are shown in Figs. 10 and 11, respectively. The upper part of each figure is the plan view, and the lower part is the side view. Comparison of the side view images in these figures shows that large-scale spanwise vortex structures are present along the entire streamwise extent of the simulated flow. The influence of the density ratio on the large-scale spanwise-orientated structures is evident in the images, as structures in case 3 have a substantially smaller vertical extent than those in case 9, at a given downstream position. In the plan view of case 3, there is an obvious streaky structure present across the span of layer. A similar structure is readily observed in the region $0 \leq x/\theta_i \leq 800$ in case 9, beyond which a regular streamwise structure is not so apparent. The visualizations of the mixing layer shown in Figs. 10 and 11 display all of the vortex structure features observed in the visualization images captured by experiments performed in the rig used by Brown and Roshko.[1,11,14]

The effect of density ratio on the large-scale turbulent vortex structures present within the mixing layer is now quantified. The vortex structures with their orientations parallel to the spanwise axis, and those with their orientations parallel to the streamwise axis, are discussed in turn.

A. Spanwise structures

Figures 12(a), 12(c), and 12(e) show typical large-scale spanwise vortex structures in the turbulent region of cases 2, 5, and 8, respectively. These structures were selected as the core of each structure is roughly coincident at $x/\theta_i \approx 750$. The figures show contour maps of the normalized spanwise averaged streamwise velocity, $\langle \tilde{u} \rangle / U_1$, and the contour lines are the spanwise averaged high-speed side molar concentration, $\langle \zeta \rangle$. The molar concentration lines provide a visual guide as to the geometry of the large-scale spanwise structure, which is quasi-two-dimensional in nature.[1,35] It is apparent that, for all values of s, the structures occupy the entire local visual thickness of the layer. The

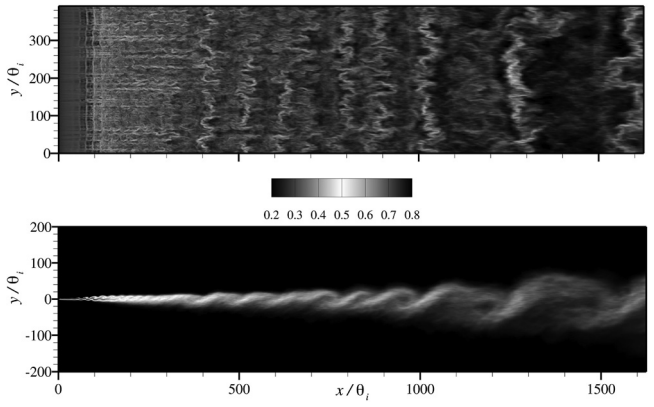

FIG. 10. Instantaneous flow visualization of case 3 ($s = 0.138$, $\lambda = 0.66$), using numerical schlieren. The upper image is the plan view, and the lower image is the side view.

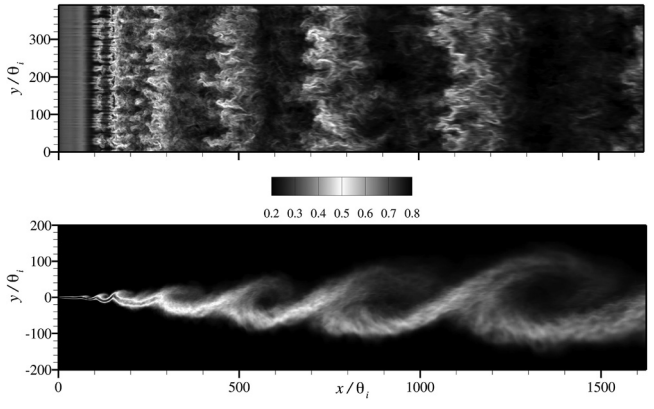

FIG. 11. Instantaneous flow visualization of case 9 ($s = 7.23$, $\lambda = 0.66$), using numerical schlieren. The upper image is the plan view, and the lower image is the side view.

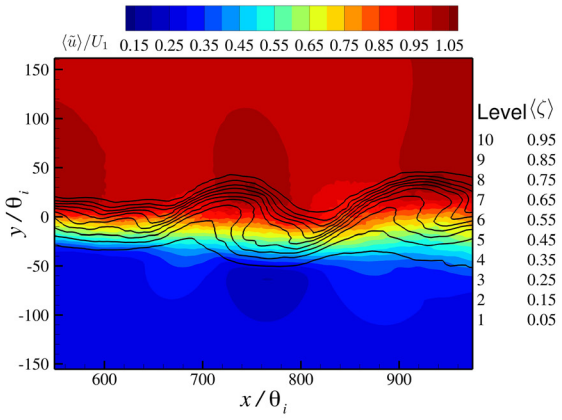

(a)Case 2, $\lambda = 0.52$, $s = 0.138$.

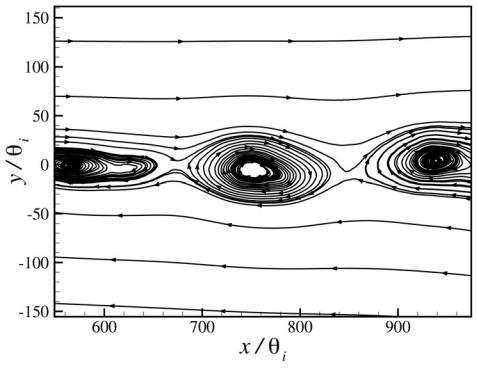

(b)Case 2, $\lambda = 0.52$, $s = 0.138$.

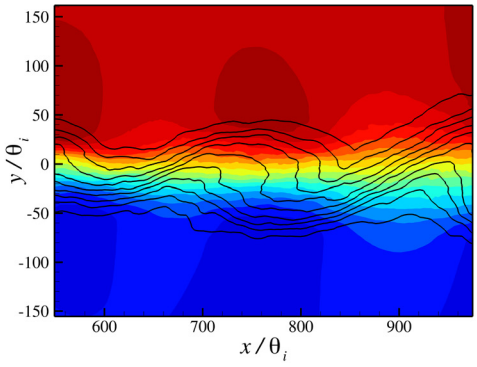

(c)Case 5, $\lambda = 0.52$, $s = 1$.

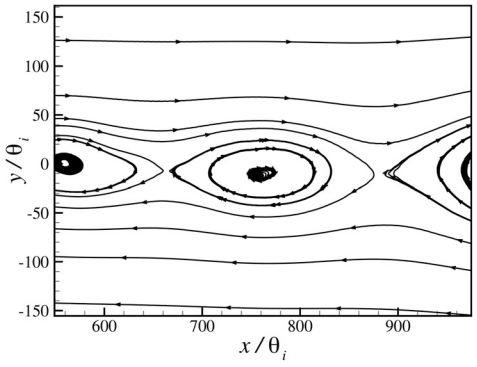

(d)Case 5, $\lambda = 0.52$, $s = 1$.

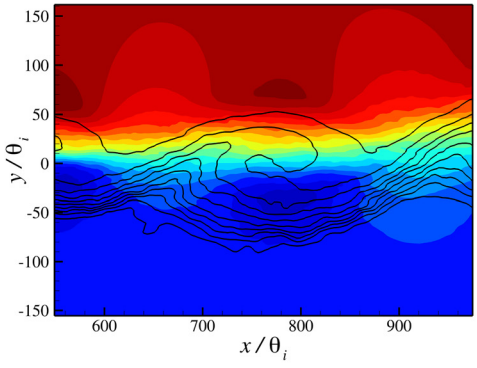

(e)Case 8, $\lambda = 0.52$, $s = 7.23$.

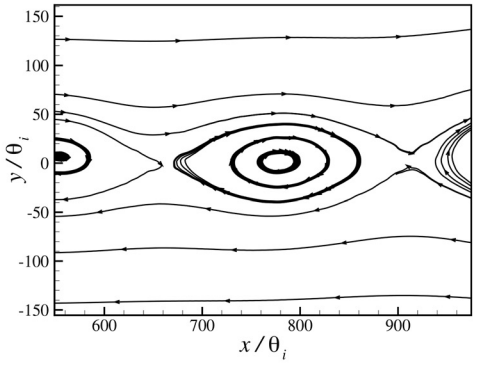

(f)Case 8, $\lambda = 0.52$, $s = 7.23$.

FIG. 12. Typical large-scale, spanwise-orientated turbulent vortex structures observed in the simulations, at $\lambda = 0.52$.

$\langle \tilde{u} \rangle / U_1$ contour maps show that, in the vertical plane of the core of each structure, there is a local overshoot in the high-speed side streamwise velocity with respect to the freestream value over the upper edge of the structure, and a local undershoot in the low-speed side streamwise velocity with respect to the freestream value over the lower edge. The local acceleration in the freestream fluid is known to correspond to the passage of a large-scale structure containing a concentrated core of spanwise vorticity,[3,4,56,57] and therefore, it can be inferred that for all values of s, the large-scale structures contain concentrated spanwise vorticity, which induces motion in the freestream flow.

The structures can be viewed in the Lagrangian frame by plotting streamlines based on the instantaneous flow field, $(\langle\tilde{u}\rangle - U_c, \langle\tilde{v}\rangle)$, and the corresponding Lagrangian streamline plots for the structures in Figs. 12(a), 12(c), and 12(e) are shown in Figs. 12(b), 12(d), and 12(f), respectively. Regardless of the value of density ratio, the core of each vortex structure has a well-defined center of rotation, which is bounded by two saddle points. The streamwise distance between the saddle points defines the spacing of a structures, l. For the single structure from cases 2, 5, and 8, shown in Fig. 12, examination of the streamwise extent occupied by each structure provides qualitative evidence that the spacing of the structures increases with s, for a given value of λ.

A more quantitative analysis of the mean structure spacing, $\bar{l}$, can be produced using three distinct methods. The first method is through interrogation of autocorrelations of the streamwise velocity fluctuations at a vertical height $y = \pm 6\theta$ at various streamwise locations.[56,57] The autocorrelations are computed from

$$C_u = \frac{\overline{u''(t)u''(t+\Delta\tau)}}{\overline{u''^2}}, \tag{15}$$

and are shown in Fig. 13 for data recorded at $x/\theta_i = 1086$ from cases 2, 5, and 8. The characteristic time is defined as the time to the first peak in the autocorrelation, and it can be seen that the values obtained for the high-speed side, τ_1, and the low-speed, τ_2, are closely matched for a given simulation. It can also be observed that, for the simulations of constant λ shown in Fig. 13, the characteristic time of the autocorrelation increases with increasing values of s. The mean structure spacing, $\bar{l}$, can be obtained from the autocorrelation data through the relationship,

$$\bar{l} \simeq U_c \tau_{12}, \tag{16}$$

where τ_{12} is the average of the characteristic times τ_1 and τ_2.[4] The second method is to produce cross correlation plots of the time series data at $y = \pm 6\theta$ for a given streamwise location. The cross correlation is computed from

$$C(\tau) = \frac{\overline{\tilde{u}_a(t)\tilde{u}_b(t+\tau_n)}}{\sqrt{u_a''^2}\sqrt{u_b''^2}}, \tag{17}$$

where $\tilde{u}_a$ and $\tilde{u}_b$ are the velocity signals recorded in the high-speed stream and low-speed stream at $y = \pm 6\theta$. The cross-correlations are shown in Fig. 14 for cases 2, 5, and 8. The characteristic time is obtained from the time between peaks in the correlation plot. For each case, the characteristic time obtained from the cross correlation data closely matches the value of τ_{12} from the autocorrelations. The third method uses the Lagrangian velocity field data shown in Figs. 12(b), 12(d), and 12(f) to directly determine the spacing of up to 200 structures per simulation, from which a mean value is obtained. All three methods produce broadly similar values for the mean structure spacing. The normalized mean structure spacing, $\bar{l}/(x - x_0)$ is shown in Fig. 15 for all nine cases studied here. Also included in Fig. 15 is the prediction of the structure spacing from a growth and entrainment model, where it was assumed that the structure spacing was invariant of s.[12] The mean structure spacing in the present simulations is clearly shown to be a function of both the density ratio, and the velocity ratio parameter. The solid lines on the figure correspond to the relationship,

$$\frac{\bar{l}}{x - x_0} = \frac{k_l \lambda}{1 + \Lambda\lambda}, \tag{18}$$

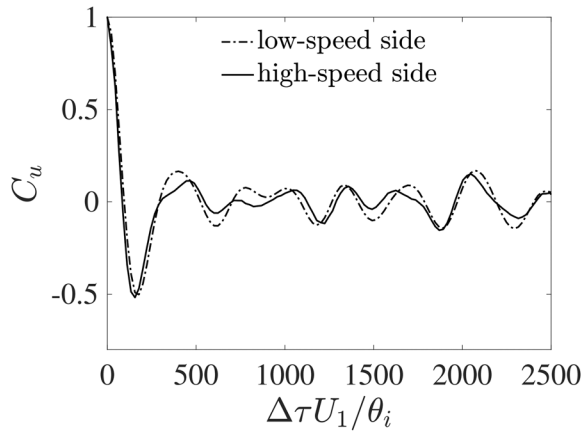

(a)Case 2, $\lambda = 0.52$, $s = 0.138$.

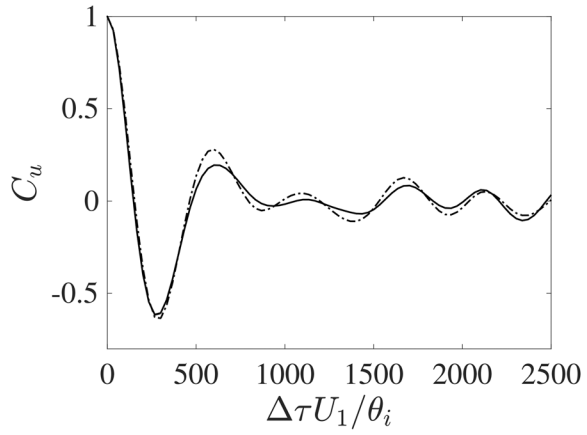

(b)Case 5, $\lambda = 0.52$, $s = 1$.

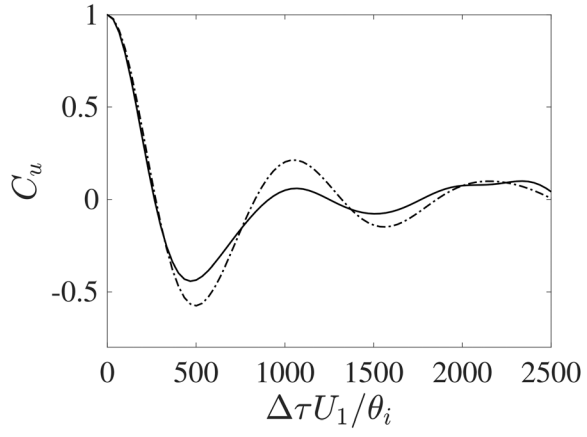

(c)Case 8, $\lambda = 0.52$, $s = 7.23$.

FIG. 13. Autocorrelations of the streamwise velocity signal recorded at $y/\theta = \pm 6$ in case 1, at $x/\theta_i = 1086$.

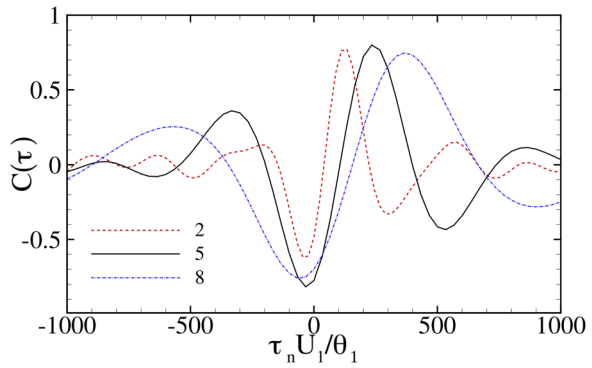

FIG. 14. Cross-correlations of the streamwise velocity signal, sampled at the same locations from which the autocorrelations of Fig. 13 were produced.

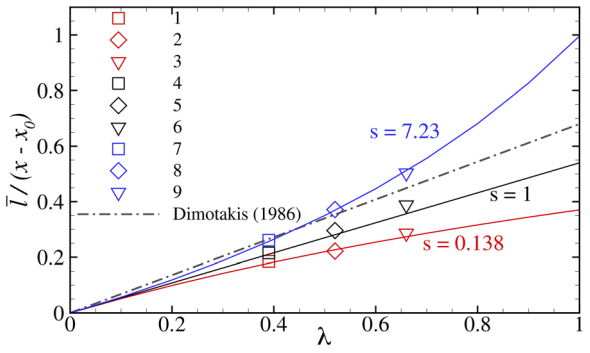

FIG. 15. Mean structure spacing in the simulations. Dashed-dotted line corresponds to the prediction of the Dimotakis entrainment model.[12] Remaining lines correspond to the predictions of Eq. (18).

where k_l is a constant. For the present simulations, $k_l = 0.54$, a value which is in good agreement with other numerical[32,35,39] and experimental studies.[1,4,58] A previous numerical study qualitatively suggested a density ratio dependency of the spanwise structure spacing for $\lambda = 0.66$, and the current findings quantify that the density ratio dependency exists over the range of λ considered here.

For all values of s and λ studied here, the spanwise structures present in the turbulent region grow continuously, with a square-root-of-time dependency.[32,39] This pattern of growth necessitates interactions between the structures in order to redistribute the spanwise vorticity within the layer, and to facilitate the overall mean self-similar growth of the flow. The interactions which occur are of the amalgamative type and of the tearing/bleeding type, which are described in detail elsewhere.[8,32]

B. Streamwise structures

Figures 16–18 show contour maps of the mean streamwise vorticity, Ω_x, for cases 6, 9, and 3, respectively ($\lambda = 0.66$). The contour maps are recorded at selected downstream locations, namely $x/\theta_i = 217$,

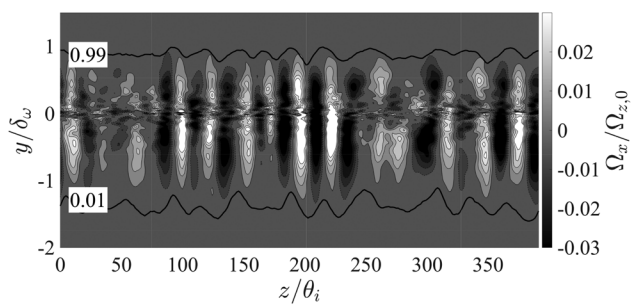

(a) $x/\theta_i = 217, P_x = 4.8$.

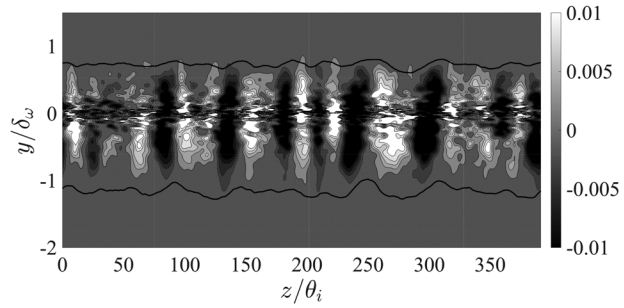

(b) $x/\theta_i = 326, P_x = 7.2$.

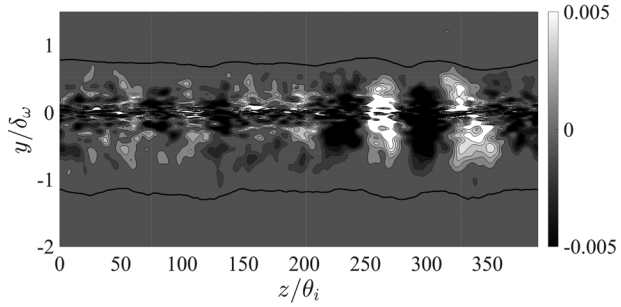

(c) $x/\theta_i = 652, P_x = 14.34$.

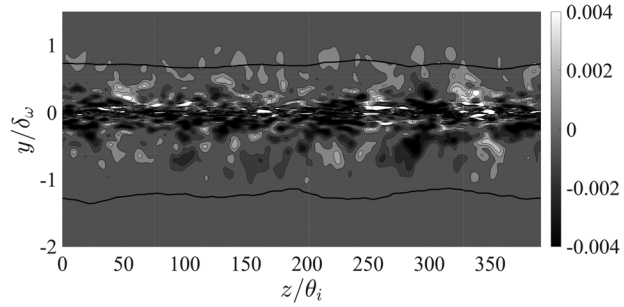

(d) $x/\theta_i = 978, P_x = 21.52$.

FIG. 16. Mean streamwise vorticity contour maps obtained from case 6, $s = 1$, $\lambda = 0.66$. Thick black lines correspond to the $\zeta = 0.01, 0.99$ high-speed side mean molar concentration lines.

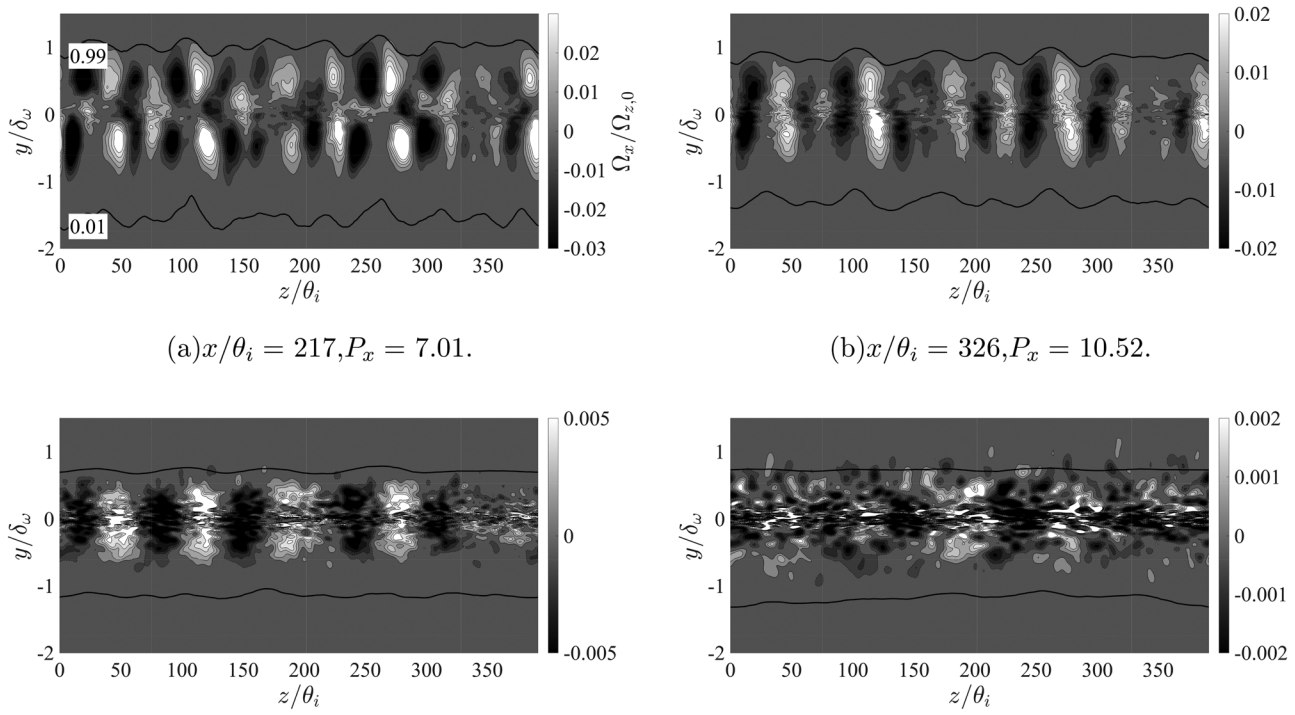

(a) $x/\theta_i = 217, P_x = 7.01.$ (b) $x/\theta_i = 326, P_x = 10.52.$

(c) $x/\theta_i = 652, P_x = 21.04.$ (d) $x/\theta_i = 978, P_x = 31.57.$

FIG. 17. Mean streamwise vorticity contour maps obtained from case 9, $s = 7.23$, $\lambda = 0.66$. Thick black lines correspond to the $\zeta = 0.01, 0.99$ high-speed side mean molar concentration lines.

326, 652, and 978. The mean streamwise vorticity is normalized by the maximum initial spanwise vorticity of the flow, $\Omega_{z,0}$. Contour lines of the mean high-speed side molar concentration, $\zeta = 0.01, 0.99$ are also plotted to show the local visual thickness of the layer across the span of the sampling station.

The streamwise vortex structure in case 6 ($s = 1$) evolves in a similar manner to that of other simulations of the laboratory mixing layer reported elsewhere.[32,35] At the first sampling plane ($x/\theta_i = 217$, $P_x = 4.8$), the streamwise vortex structure has evolved into a single row of alternating sign streamwise vortices along the span of the layer. The streamwise vortices occupy, in a mean sense, the local visual thickness of the layer, and the undulations in the visual thickness along the span of the flow correspond to the interfaces between pairs of counter-rotating streamwise vortices. At the next measurement station ($x/\theta_i = 326$, $P_x = 7.2$), the number density of the structures has reduced; examples of two like-signed vortices annihilating a vortex of opposite sign can be observed at $z/\theta_i = 100, 260$ in Fig. 16(b). At the third sampling station ($x/\theta_i = 652$, $P_x = 14.34$), the number density of the streamwise vortices has reduced further, and the vortices have begun to lose their coherence; notable are the four strong vortices occupying $210 < z/\theta_i < 370$, which have retained their coherence. By the final sampling plane ($x/\theta_i = 978$, $P_x = 21.52$), all of the streamwise vortices have lost their coherence, and they are almost indiscernible.

The mean streamwise vorticity maps extracted from case 9 ($s = 7.23$) are shown in Fig. 17. At $x/\theta_i = 217$ ($P_x = 7.01$), the three-tiered clusters are in the process of realignment to a single row of alternating sign streamwise vortices, and this process has been completed by $x/\theta_i = 326$ ($P_x = 10.52$). In both Figs. 17(a) and 17(b), it is apparent that the streamwise vortices are biased toward the low-density fluid on the high-speed side. It is also interesting to note that there is a marked tilt in the orientation of the streamwise vortices with respect to the vertical axis at $x/\theta_i = 326$, such that pairs of neighboring negative/positive vortices tilt toward each other on the low-density side, and away from each other on the high-density side. The tilting effect is most apparent for the pairs of stronger streamwise vortices. At $x/\theta_i = 652$ ($P_x = 21.04$), the streamwise vortices begin to lose their coherence, and the effect of the tilting is less apparent. The vortices do, however, retain their bias toward the low-density stream. Finally, at $x/\theta_i = 978$ ($P_x = 31.57$) the streamwise vortices have lost their coherence but the overall distribution of the streamwise vorticity field remains biased toward the low-density side.

The evolution of the mean streamwise vorticity field in case 3 ($s = 0.138$) is shown in Fig. 18. The three-tiered clusters present at $x/\theta_i = 217$ ($P_x = 3.76$) unwrap to form a single row of streamwise vortices by $x/\theta_i = 326$ ($P_x = 5.64$). The number density of the streamwise vortices decreases with downstream distance, implying that interactions take place between them, but the structures largely retain their coherence to the furthest downstream measurement station. When the single row of streamwise vortices has formed, the structures are initially biased toward the low-density stream (the low-speed side for $s = 0.138$), but this bias diminishes with

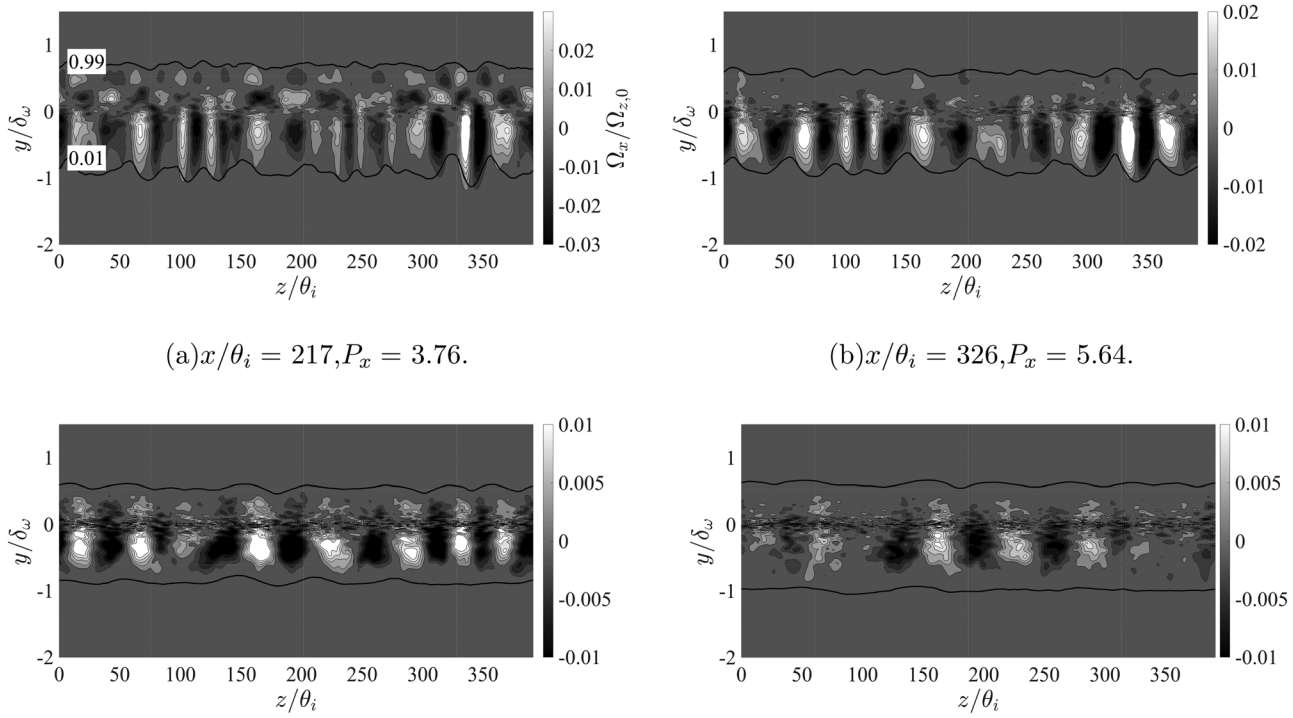

FIG. 18. Mean streamwise vorticity contour maps obtained from case 3, $s = 0.138$, $\lambda = 0.66$. Thick black lines correspond to the $\zeta = 0.01, 0.99$ high-speed side mean molar concentration lines.

downstream distance. There is also some evidence for the streamwise vortices being tilted with respect to the vertical axis, but this effect is not as pronounced as it is for the high-density ratio flow, as is apparent in Fig. 17.

At seven selected downstream locations, $x/\theta_i = 44$, 109, 217, 326, 652, 978, and 1304, the absolute maximum value of Ω_x in each streamwise vortex present in the flow is recorded, and an average maximum value is obtained. The obtained value, $\Omega_{x,\max}$ is normalized by the local peak spanwise vorticity, $\Omega_{z,\max}$, and is plotted in Fig. 19, as a function of the pairing parameter. The simulations are grouped in each subfigure by velocity ratio parameter value, to aid the clarity of the presentation. For all cases, the residual streamwise vorticity from the upstream flow is amplified to a maximum of approximately 30% of the local maximum spanwise vorticity, following which the peak magnitude of the streamwise vorticity decays. The maximum ratio of $\Omega_{x,\max}/\Omega_{z,\max}$ is largely invariant of both s and λ, and the predicted value is in excellent agreement with previous uniform density experimental measurements.[15,16] Under the assumption that the local maximum mean spanwise vorticity is approximately equivalent to the local maximum mean streamwise velocity gradient, i.e., $\Omega_{z,\max} \approx \partial U/\partial y|_{\max}$, it can be inferred from Fig. 3 that the magnitude of the spanwise vorticity is inversely proportional to downstream distance. Given that the ratio $\Omega_{x,\max}/\Omega_{z,\max}$ decreases from its maximum value with increasing downstream distance implies that the streamwise vorticity decays more rapidly than the spanwise vorticity. The more rapid decay of the streamwise vorticity when compared to the spanwise component was observed in uniform density experimental measurements,[15] and the finding is generalized to variable density flows here.

The average value of the streamwise vorticity, $\Omega_{x,ave}$, inside the visual thickness of the layer across the span is computed by taking the mean of the quantity inside the mean $\zeta = 0.01, 0.99$ concentration lines. For all cases considered here, the average streamwise vorticity in a y–z plane at any given downstream measurement station, $\Omega_{x,ave}/\Omega_{z,0}$ is negligibly small, as would be expected for a nominally two-dimensional mixing layer. Similarly, the total mean circulation on the cross-plane, Γ_c, obtained by taking the surface integral of the streamwise vorticity within the visual thickness, is also vanishingly small.

The action of the streamwise vortices is to impart a cross-stream transfer of streamwise momentum across the layer. This is manifested in the wrinkling of the mean velocity field, and associated Reynolds stresses. Examples of the wrinkling of these fields are provided in Fig. 20, where cross-plane contour maps of the normalized mean streamwise velocity field, U/U_1, and the normalized primary Reynolds shear stress, R_{12}, are plotted at $x/\theta_i = 326$ in Cases 3, 6, and 9. For all density ratios, the mean streamwise velocity field is wrinkled by the streamwise vortices—a peak in the streamwise velocity map corresponds to the interface between two streamwise vortices with a common upflow, and a valley corresponds a pair of streamwise vortices with a common downflow. The large spanwise variations caused by the wrinkling, and the localized peaks in the primary Reynolds shear stress contour maps are indicative of the action of a stationary

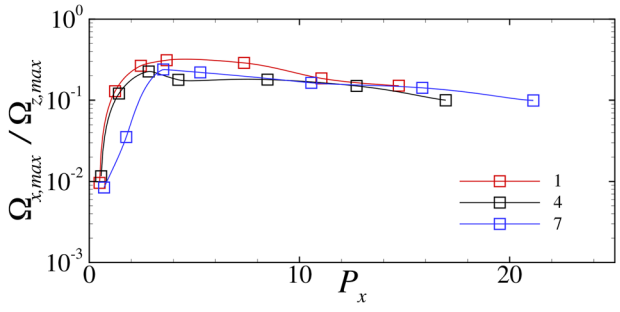

(a)$\lambda = 0.39$.

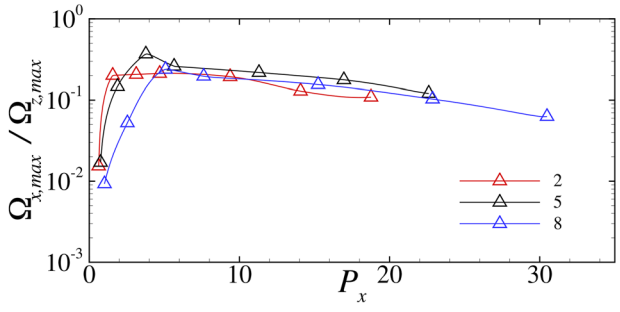

(b)$\lambda = 0.52$.

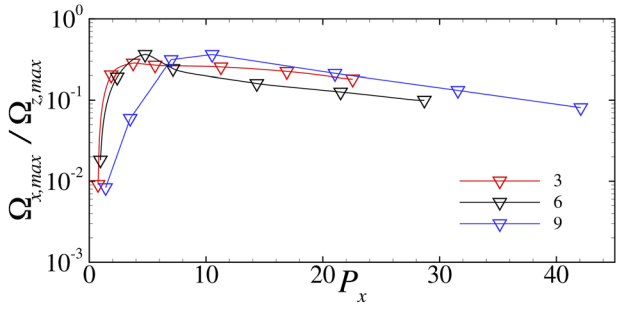

(c)$\lambda = 0.66$.

FIG. 19. Relative strength of the streamwise vortex structure to the local maximum mean spanwise vorticity, for all simulations presented here.

streamwise vortex structure. The trends observed in these maps for all density ratios are in excellent agreement with uniform density experiments,[19] uniform density simulations of the laboratory mixing layer,[32–35] and previous LES of the laboratory mixing layer at variable density conditions.[39]

Further quantitative information on the evolution of the streamwise structure can be obtained from two-point correlations of the streamwise velocity field along the ray of spanwise-averaged mixing layer centerline, i.e., the vertical location where $\langle U \rangle = U_c$. The two-point correlation is obtained through

$$C_{uu}(\Delta z) = \frac{\overline{u''(z)u''(z+\Delta z)}}{\overline{u''(z)u''(z)}}, \tag{19}$$

and the correlation plots from cases 3, 6, and 9 are shown in Fig. 21. The separation distance to the first peak in the correlation can be interpreted as the spanwise wavelength of the streamwise vortex structure. In the range of the pairing parameter $2 < P_x < 16$, the correlation plots have a reasonably well-defined periodicity. Beyond $P_x \approx 16$, the correlations display no clear evidence for a periodic feature across the span, and this behavior occurs for all values of the density ratio. The loss of apparent periodicity in the spanwise correlations demonstrates that the streamwise structure loses its coherence beyond $P_x > 16$. Similar findings are obtained for all other cases considered here, and the results presented here are in good agreement with other uniform density simulations of the laboratory mixing layer.[35]

The spanwise wavelength of the streamwise structure, b, is obtained by computing the mean distance between like-signed streamwise vortices in the cross-plane contour maps of mean streamwise vorticity, and comparing the value with that obtained from the spanwise correlation data. The spanwise wavelength is then normalized by the local vorticity thickness, and plotted as a function of non-dimensional streamwise distance in Fig. 22(a). All simulations have a ratio of b/δ_ω, which asymptotes to a value of approximately unity at $x/\theta_i \approx 500$. A more representative normalization of the downstream distance is the pairing parameter, which accounts for the effects of both density ratio and velocity ratio on the flow evolution. When plotted as a function of P_x in Fig. 22(b), it can be seen that the streamwise structure wavelength attains the asymptotic value beyond $P_x \approx 10$, independent of both the velocity ratio and the density ratio. The streamwise structure therefore obtains its asymptotic lengthscale after the second generation of pairings between primary structures, which corresponds to the interaction which triggers the transition to turbulence in the current simulations. The finding shown here supports previous experimental evidence of the variable density mixing layer from Bernal and Roshko, who obtained an asymptotic ratio of $b/\delta_\omega = 0.80 \pm 0.14$ for $s = 7, \lambda = 0.45$. Uniform density experiments have obtained asymptotic values of $b/\delta_\omega = 1.28 \pm 0.21$ for $\lambda = 0.25$,[15] and $b/\delta_\omega = 1.28$–1.25 for $\lambda = 1$.[17]

VI. VORTICITY DYNAMICS

The vorticity equation is obtained by taking the curl of the momentum equation. For a three-dimensional flow, the vorticity equation can be written in vector form as

$$\frac{D\boldsymbol{\omega}}{Dt} = -\boldsymbol{\omega}(\nabla \cdot \boldsymbol{u}) + (\boldsymbol{\omega} \cdot \nabla)\boldsymbol{u} + \frac{1}{\rho^2}(\nabla\rho \times \nabla p) + \frac{1}{Re}(\nabla^2\boldsymbol{\omega}). \tag{20}$$

There are four different mechanisms which can alter the development of the vorticity field—thermal expansion, $-\boldsymbol{\omega}(\nabla \cdot \boldsymbol{u})$, vortex stretching, $(\boldsymbol{\omega} \cdot \nabla)\boldsymbol{u}$, viscous diffusion, $\frac{1}{Re}(\nabla^2\boldsymbol{\omega})$, and baroclinic torque, $\frac{1}{\rho^2}(\nabla\rho \times \nabla p)$. For an isothermal, variable density flow, the thermal expansion term is zero. For the low Richardson number flows considered here, the effect of buoyancy is negligible and hence the gravitational terms can be neglected. Application of this assumption to the fluid momentum equation simplifies the baroclinic torque term to

$$\dot{\boldsymbol{\omega}}_b = \frac{\nabla\rho \times \nabla p}{\rho^2} = -\frac{1}{\rho}\nabla\rho \times \boldsymbol{a}, \tag{21}$$

where $\boldsymbol{a}$ is the material acceleration. Baroclinic torque therefore arises in the low-speed, low Richardson number variable density mixing

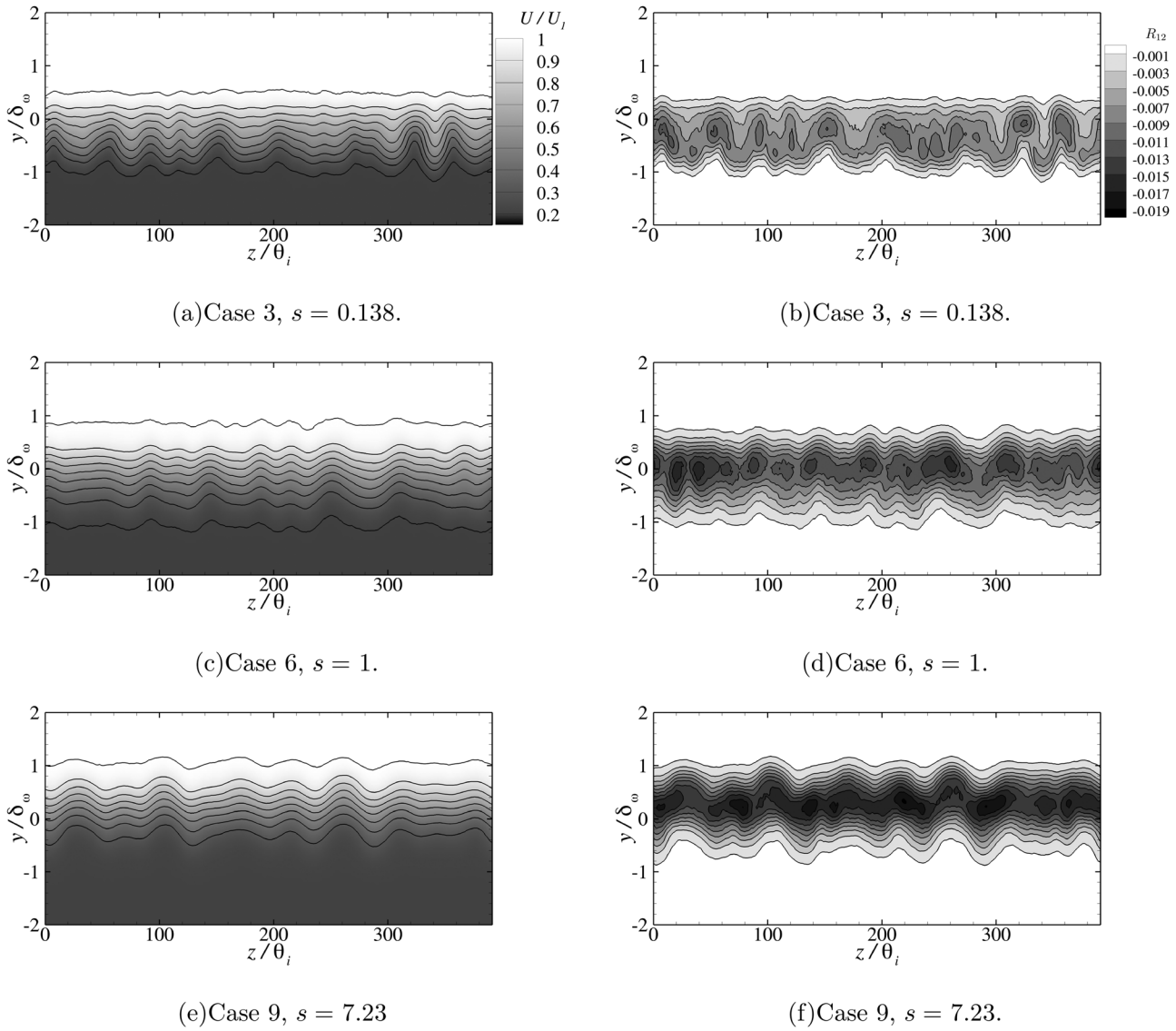

FIG. 20. Cross-plane contour maps of mean streamwise velocity (left), and primary Reynolds shear stress (right), recorded at $x/\theta_i = 326$ in cases 3, 6, and 9 ($\lambda = 0.66$).

layer owing to the misalignment of the material acceleration and density gradient vectors.

A. Spanwise vorticity

Figure 23 shows an instantaneous snapshot of the spanwise vorticity field, ω_z, at an arbitrary instant in time from case 6 ($s = 1$, $\lambda = 0.66$). The single-plane image was recorded at mid-span, and shows the spanwise vorticity distribution in the layer as the flow rolls up into discrete K–H vortices. The spanwise vorticity is normalized by the initial spanwise vorticity of the layer, $\omega_{z,0}$. At $x/\theta_i \approx 80$, a K–H vortex has a concentrated core of spanwise vorticity, formed from the roll up of spanwise vorticity present in the upstream vortex sheet. The image in Fig. 23 is used as a reference for the spanwise vorticity distribution within the initial region of the flow, for comparison with the spanwise vorticity distributions for cases 3 and 9 in Fig. 24. The initial roll-up of the mixing layer is highlighted as a means to demonstrate the effect of baroclinic torque on the flow, as the density gradients are steepest in this region.

Figure 24(a) shows the instantaneous spanwise vorticity distribution at an arbitrary instant in time from case 3 ($s = 0.138$, $\lambda = 0.66$). In the K–H vortices present at $x/\theta_i \approx 90$ and 120, there is a clear reduction in the magnitude of the spanwise vorticity present on the upper side of each vortex, and an increase in its magnitude toward the low-speed side, when compared to the uniform density case in 23. The corresponding $z-$component of the baroclinic torque distribution, $\dot{\omega}_{b,z}$, is shown in Fig. 24(b). The enhanced magnitude of the spanwise vorticity on the low-speed side corresponds to band of

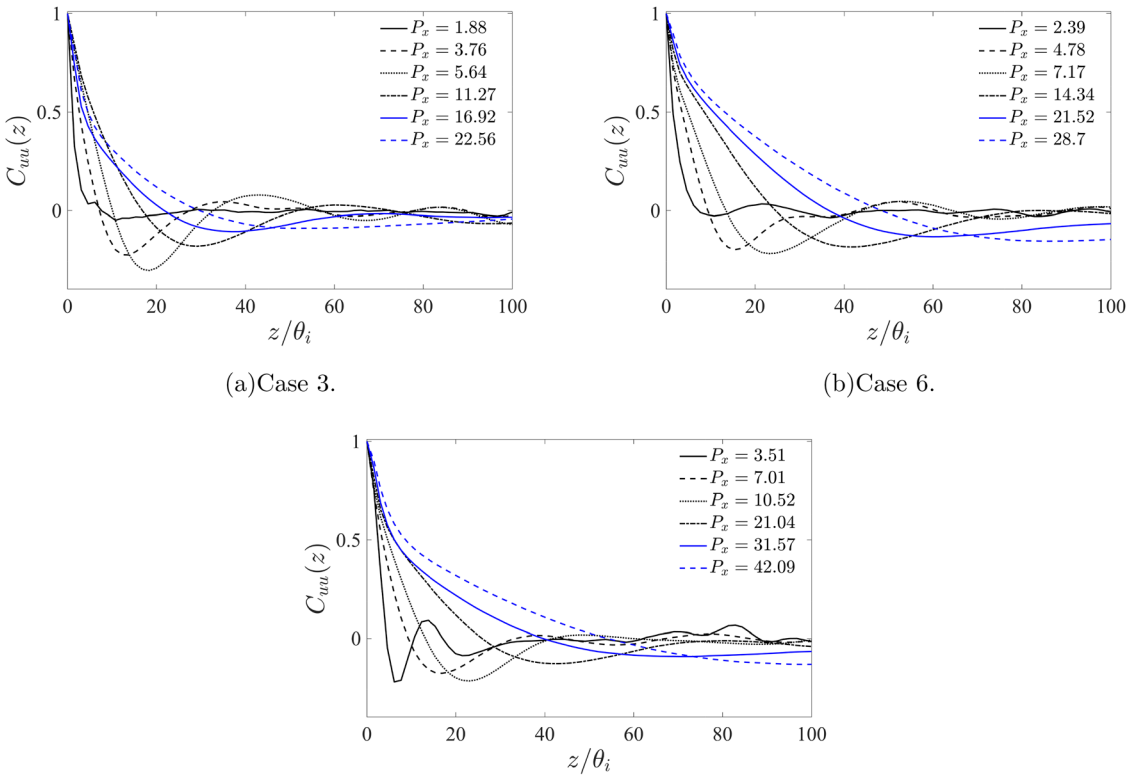

(a)Case 3. (b)Case 6.

(c)Case 9.

FIG. 21. Two-point spatial correlations of the streamwise velocity across the span of the mixing layer, at various streamwise locations. Correlation data recorded along the ray where $\langle U \rangle = U_c$.

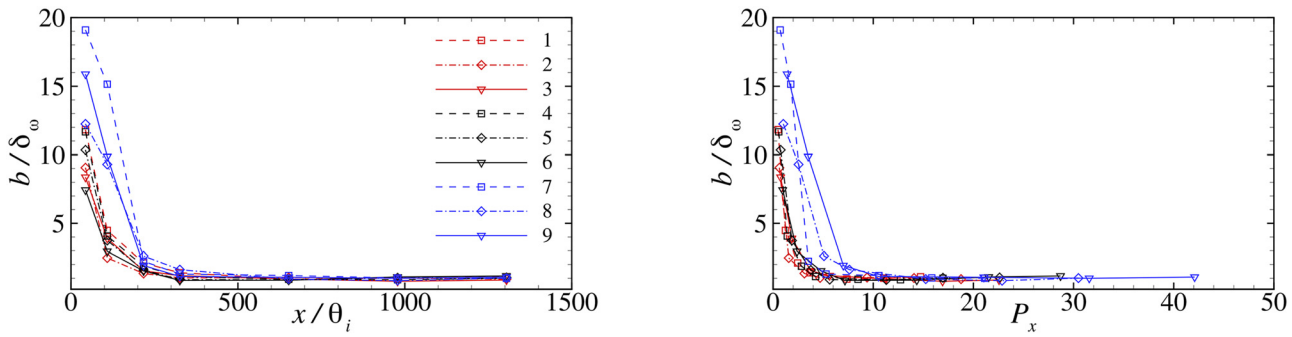

(a)Streamwise distance as x/θ_i. (b)Streamwise distance as P_x.

FIG. 22. Evolution of the spanwise wavelength of the streamwise vortex structure, b, as a function of downstream distance.

negative baroclinic torque, which generates additional negative spanwise vorticity. Toward the upper side of the vortex, there are regions of positive baroclinic torque, which produce positive spanwise vorticity that diminishes the strength of the vortex on the high-speed side. The interconnecting braid regions are dominated by strong negative vorticity generation, with smaller fingers of positive vorticity generation flanking it.

A typical instantaneous snapshot of the K–H roll-up in case 9 ($s = 7.23$, $\lambda = 0.66$) is shown in Fig. 24(c). The spanwise vorticity is enhanced with respect to that present in case 6 toward the high-speed

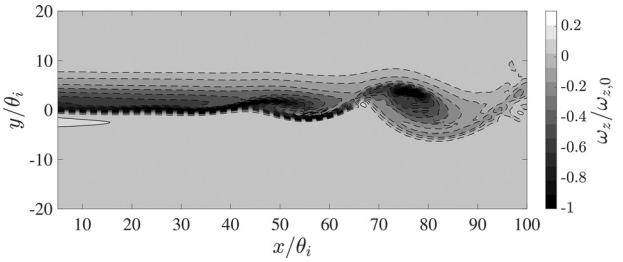

FIG. 23. Instantaneous spanwise vorticity contours in case 6, selected at an arbitrary instant in time.

side of the vortex, and a region of positive spanwise vorticity is present on the underside. The corresponding baroclinic torque plot of Fig. 24(d) shows a pronounced region of negative torque on the upper side of the vortex, and a region of positive torque on the underside. In the interconnecting braid region, strong positive spanwise vorticity generation is present, with a smaller region of negative spanwise vorticity generation flanking it. The maps presented here display excellent agreement with the findings of Soteriou and Ghoniem, who studied the vortex dynamics of spatially developing mixing layers confined to two-dimensional boxes.[31]

More quantitative information on the baroclinic torque is obtained from analysis of the normalized spanwise component of the mean baroclinic torque, $\dot{\Omega}_{b,z}/\Omega^2_{z,0}$, at various downstream locations. Two such locations are shown in Fig. 25, namely $x/\theta_i = 100$, and 1000. These measurement positions are chosen as they reflect the influence of the torque on the near-field flow, and the fully developed turbulent flow, respectively. The results are grouped by density ratio, where Figs. 25(a) and 25(b) show $s = 0.138$ simulation data, and Figs. 25(c) and 25(d) show the $s = 7.23$ results. For the low-density ratio calculations, the near-field negative torque on the low-speed side is substantially stronger than the positive vorticity generation in the high-speed stream, for all values of λ. As the flow reaches a self-similar state in Fig. 25(b), the magnitude of the generation rate has dropped by an order of magnitude when compared to the near-field values, and the rate of generation is roughly equivalent in both streams. The continued generation of positive spanwise vorticity on the high-speed side in the far-field is the likely cause of the positive primary Reynolds shear stress observed on the high-speed side in Fig. 6(d). For the high-density ratio simulations in Fig. 25(c), the magnitudes of the vorticity generation in both streams is roughly equivalent, but with the sign of the generation in each stream when reversed when compared to the $s = 0.138$ calculations. In the far-field plots of Fig. 25(d), the positive spanwise vorticity generation on the low-speed side has reduced to near-zero values, whilst on the high-speed side the negative spanwise vorticity generation rate has dropped by an order of magnitude when compared to the near-field profiles. The generation of spanwise baroclinic torque therefore falls into two principal components; vorticity production by the misalignment of the density gradient and material acceleration in the cores of the large-scale structures, and vorticity production by the misalignment of the density gradients and material acceleration in the braid region. The cyclic passage of the large-scale structures and braids over a long statistical sample leads to mean plots shown in Fig. 25.

B. Streamwise vorticity

The streamwise component of baroclinic torque, $\dot{\omega}_{b,x}$ also arises from the misalignment of the density gradient and material

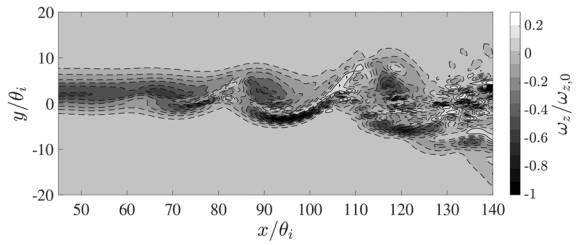

(a)$\omega_z/\omega_{z,0}$, Case 3, $s = 0.138$, $\lambda = 0.66$.

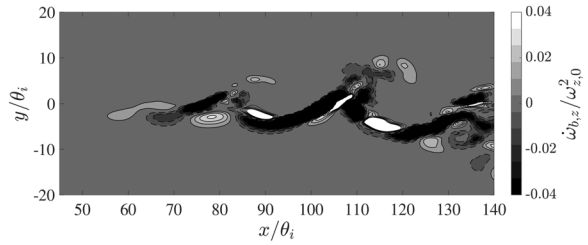

(b)$\dot{\omega}_{b,z}/\omega^2_{z,0}$, Case 3, $s = 0.138$, $\lambda = 0.66$.

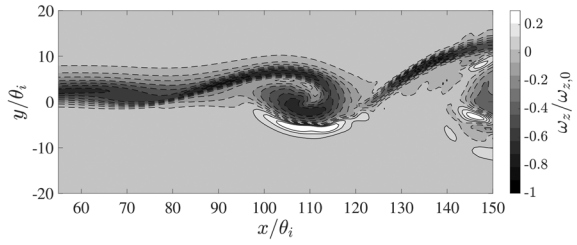

(c)$\omega_z/\omega_{z,0}$, Case 9, $s = 7.23$, $\lambda = 0.66$.

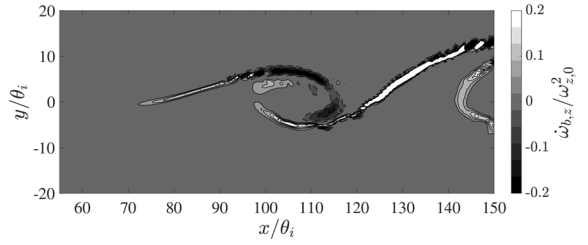

(d)$\dot{\omega}_{b,z}/\omega^2_{z,0}$, Case 9, $s = 7.23$, $\lambda = 0.66$.

FIG. 24. The influence of baroclinic torque on the K–H roll-up in the variable density mixing layer.

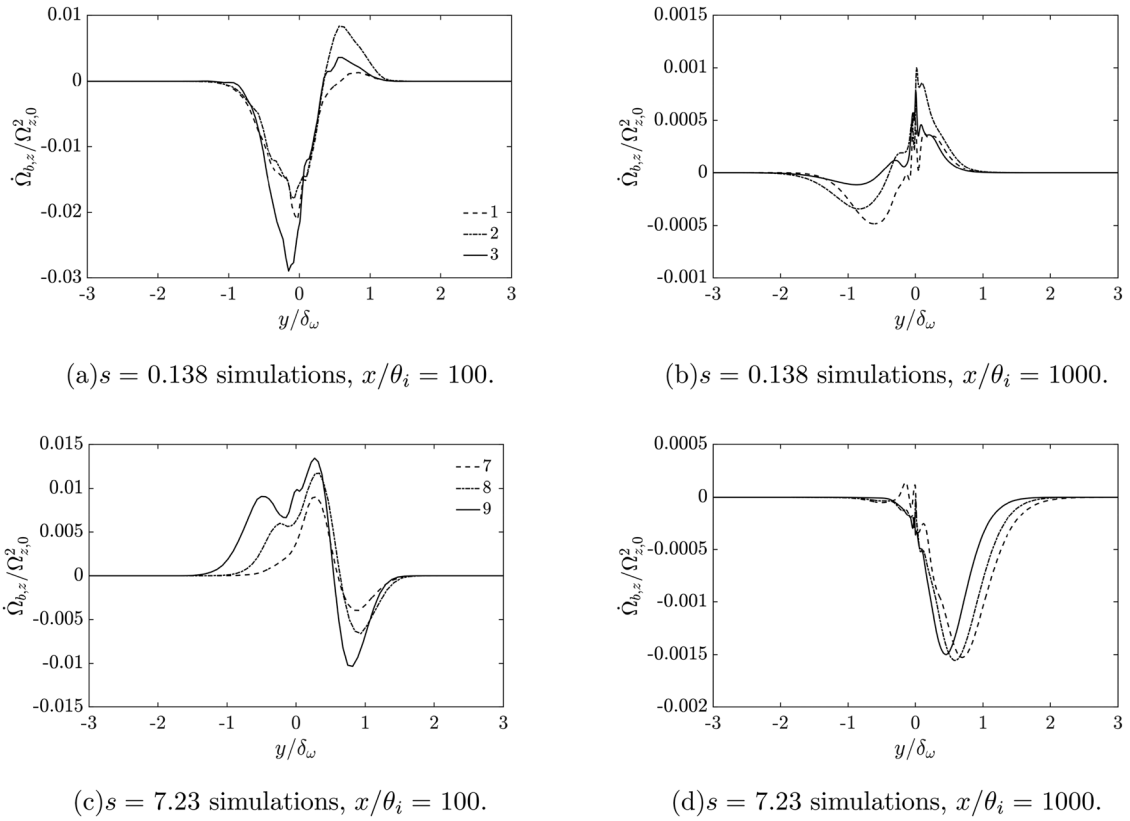

(a)$s = 0.138$ simulations, $x/\theta_i = 100$. (b)$s = 0.138$ simulations, $x/\theta_i = 1000$.

(c)$s = 7.23$ simulations, $x/\theta_i = 100$. (d)$s = 7.23$ simulations, $x/\theta_i = 1000$.

FIG. 25. Profiles of mean spanwise vorticity, and mean baroclinic torque, in the near-field and self-similar turbulent regions of the variable density mixing layer.

acceleration. The mechanism by which $\dot{\omega}_{b,x}$ arises, however, is more complex. It has been established that the streamwise structure loops back and forth between neighboring spanwise vortices in the interconnecting braid region.[14] The streamwise vortices are therefore influenced by the vertical motion induced by the rotation of the spanwise vortex structures, and also by the induced spanwise motions from the streamwise vortices themselves. To highlight the production of streamwise baroclinic torque, instantaneous images are presented from within the braid region of cases 3 and 9. The braid regions are chosen for interrogation as only a single row of streamwise vortices is present in the braids.[14,59]

An instantaneous map of the high-speed side molar concentration is shown in Fig. 26(a) for case 9. The map was recorded at $x/\theta_i = 326$, $P_x = 10.52$. The molar concentration map is to be used as a guide to determine the spanwise positions of the streamwise vortices, which can be inferred from the local preferential entrainment—an excess of high-speed side fluid corresponds to the location of a pair of streamwise vortices with a common downflow, and an excess of low-speed side fluid corresponds to the location of a pair of streamwise vortices with a common upflow. There is a pair of strong streamwise vortices present in the region $150 \leq z/\theta_i \leq 190$, which preferentially entrain fluid from the low-speed side. The streamwise vortex on the left of the pair has a negative rotational sense, and the vortex on the

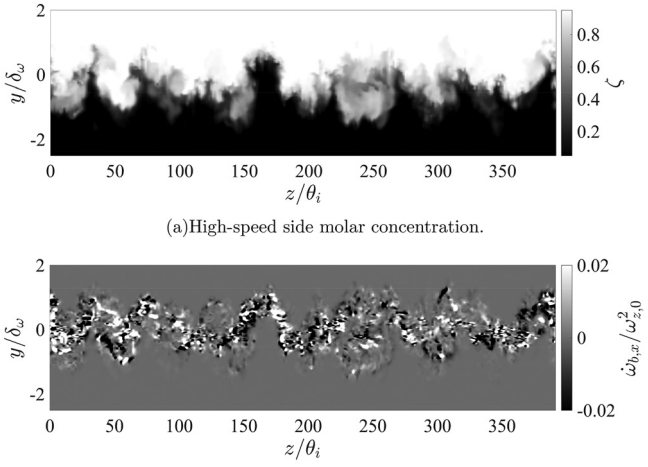

(a)High-speed side molar concentration.

(b)Normalised baroclinic torque.

FIG. 26. Contour maps of highlighting the instantaneous baroclinic torque from case 9, $s = 7.23$, $\lambda = 0.66$, recorded at $x/\theta_i = 326$, $P_x = 10.52$. Captured images are recorded in the interconnecting braid region between large-scale, spanwise orientated structures.

right has a positive rotational sense. In the corresponding $\dot{\omega}_{b,x}$ map in Fig. 26(b), it can be seen that there is a strong negative torque imparted on the left-side vortex of the pair, and a strong positive torque imparted on the right-side vortex of the pair. For both streamwise vortices, the corresponding torque is inclined to the vertical. The other streamwise vortex pairs in the image show roughly similar trends in the baroclinic torque.

A typical instantaneous map of high-speed side molar concentration in the braid region of case 3 at $x/\theta_i = 326$, $P_x = 5.64$, is shown in Fig. 27(a). Similar features are observed to those of case 9, where local preferential entrainment from one of the freestreams occurs owing to the common flow sense of a pair of streamwise vortices. Here we focus on the streamwise vortex pair at $30 \leq z/\theta_i \leq 70$, where there is preferential entrainment from the low-speed stream. As with case 9, the left-hand vortex of the pair has a negative rotational sense, and the right-hand vortex of the pair has a positive rotational sense. The corresponding map of $\dot{\omega}_{b,x}$ in Fig. 27(b) shows that a positive baroclinic torque is imparted on the streamwise vortex with a negative rotational sense, and that a negative baroclinic torque is imparted on the streamwise vortex with a positive rotational sense. The baroclinic torque map is inclined with respect to the vertical axis as noted for case 9, but the effect of the baroclinic torque on the streamwise structure in the low-density ratio flow is opposite to its effect on the high-density ratio flow, which is a result of the change in direction of the density ratio caused by flipping the constituent gases between the freestreams. For both cases shown here, and all others considered in this study, the peak values of $\dot{\omega}_{b,x}$ are an order of magnitude lower than those of $\dot{\omega}_{b,z}$ at the same downstream location.

The maps of the mean streamwise component of baroclinic torque, $\dot{\Omega}_{b,x}/\Omega^2_{z,0}$ are shown in Fig. 28 for cases 9 and 3 at $x/\theta_i = 326$. In a mean sense, there is preferential generation of negative streamwise vorticity in case 9, and preferential generation of positive streamwise vorticity in case 3. The streamwise vorticity is generated in such a

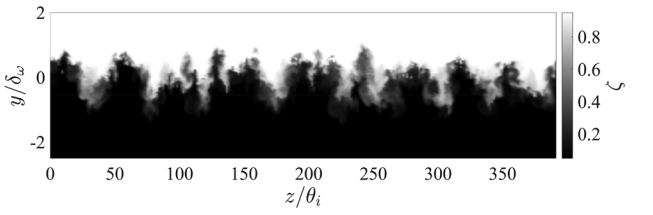

(a)High-speed side molar concentration.

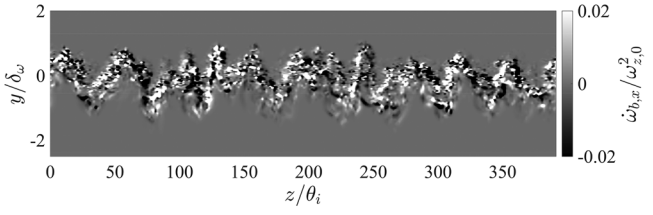

(b)Normalised baroclinic torque.

FIG. 27. Contour maps highlighting the instantaneous baroclinic torque from case 3, $s = 0.138$, $\lambda = 0.66$, recorded at $x/\theta_i = 326$, $P_x = 5.64$. Images are recorded in the interconnecting braid region between large-scale, spanwise orientated structures.

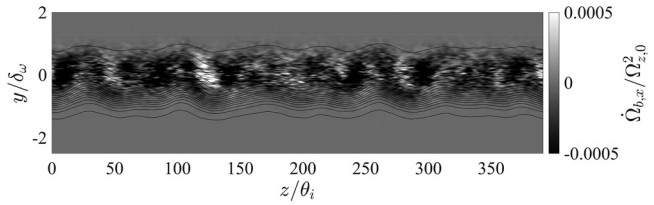

(a)Case 9, $s = 7.23$.

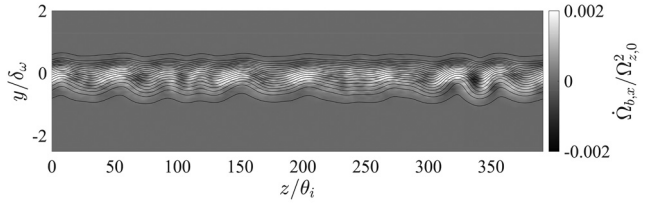

(b)Case 3, $s = 0.138$.

FIG. 28. Contour maps of mean streamwise baroclinic torque, normalized by the square of the initial mean spanwise vorticity in the layer.

manner that the resultant mean streamwise vortices, shown in Fig. 17(b) for case 9, and Fig. 18(b) for case 3, are inclined with respect to the vertical, with the effect being more pronounced on the high-density ratio case. It is interesting to note, however, that the generation of additional streamwise vorticity owing to the differing density between the freestreams does not have a substantial influence on either the initial evolution of the streamwise vortices, or on the downstream location at which the streamwise vortices lose their coherence.

VII. DISCUSSION

The results presented above provide new information on the nature of the organized structure in the turbulent plane mixing layer, subject to large variations in the density ratio between the freestreams. We now discuss these results in the context of the archival literature.

For the present simulations, where the initial conditions are representative of the clean initial conditions found in laboratory experiments of the plane turbulent mixing layer, it has been shown that the large-scale, quasi-two-dimensional structure is present across the range of s and λ studied. The structures are typical of those first observed by Brown and Roshko,[1] such that large spanwise-orientated vortex structures occupy the entire local visual thickness of the layer, and a secondary streamwise structure rides along with them.[60] The spanwise structures persist to the highest local Reynolds numbers computed in each simulation, and the streamwise structures, which are stationary in a mean sense, persist well into the downstream region of $x/\theta_i \sim 1000$ that is typically considered to represent fully-developed, self-preserving turbulent flow.[61]

The dynamical significance of the large-scale, spanwise-orientated turbulent vortex structures was quickly recognized by the research community, and their presence was observed both in flow visualization images,[3,6,7,64] and in velocity measurements of the mixing layer flow field.[3,56,57,64] In spite of the apparent ubiquity of structures across a range of Reynolds numbers, and a range of upstream flow conditions, comprehensive data on the topology of the structures as a function of both the density ratio and the velocity ratio parameter is, to the

TABLE II. Measurements of normalized spanwise vortex structure spacings available in the literature. Values by Koochesfahani and Dimotakis were made from both autocorrelation and cross correlation measurements. Other autocorrelation measurements obtained in the low-speed stream. Data from Bernal, and Hernan and Jimenez, obtained from experiments performed in the same facility as Brown and Roshko.

Study	s	λ	Measurement	$\bar{l}/\delta_\omega$	$\bar{l}/(x-x_0)$	$\bar{l}/\delta_{viz}$
Spencer and Jones[62]	1	0.25	Spectra	3.3	···	···
Spencer and Jones[62]	1	0.54	Spectra	3.8	···	···
Brown and Roshko[1]	7	0.45	Visualization	2.9	0.3	···
Brown and Roshko[1]	1/7	0.45	Visualization	3.5	0.21	···
Dimotakis and Brown[3]	1	0.65	Autocorrelation	3.1–5.0	···	···
Koochesfahani *et al.*[4]	1	0.66	Autocorrelation	3.9	···	···
Bernal[63]	1	0.45	Visualization	3	0.24	1.41
Hernan and Jimenez[8]	1	0.45	Visualization	···	0.26	1.7
Browand and Troutt[57]	1	0.39–0.81	Autocorrelation	$0.54\lambda + 4.0$	···	···
Hermanson and Dimotakis[10]	1	0.428	Visualization	···	···	1.66

knowledge of the authors, absent in the literature. The available data on the spacing of the large-scale spanwise structures is provided in Table II, and normalized as described in each article; through the vorticity thickness, δ_ω, the distance from the virtual origin, $x - x_0$, and the visual thickness of the layer, δ_{viz}, where available. In Table II, the measurement column indicates the method through which the mean structure spacing was determined. The lack of availability of comprehensive information on the mean structure spacing, has rendered difficult the ability to determine if an appropriate lengthscale is present in the flow to produce a description of the mean structure spacing that is invariant of s and λ. In addition to the lack of experimental data, issues with the obtained measurements have added to the difficulty. The use of hot-wire anemometry to produce spectra and/or autocorrelations of the mixing layer from which the mean structure spacing is inferred has been used widely.[3,4,56,57] As noted by Koochesfahani *et al.*,[4] however, recording measurements in only one of the mixing layer streams will lead to an error in the prediction of $\bar{l}$, owing to the process of vortex amalgamation in the layer and the resultant acceleration of the participating vortex nearer the high-speed side, and the deceleration of the participating vortex toward the low speed side. The values quoted in Table II from the study of Browand and Troutt were produced from autocorrelation measurements in the low-speed stream,[57] and they noted that using the average value of the characteristic time from autocorrelations recorded in both streams reduced the mean structure spacing value by up to 15%. Similar overestimation of the mean spacing may be apparent in the measurements of Dimotakis and Brown, who also measured autocorrelations in the low-speed stream. The spectra of Spencer and Jones, recorded on the outer extremes of their mixing layer, show peaks of varying frequency, dependent on the stream in which the measurement was taken, i.e., higher frequency in the high-speed stream, and lower frequency in the low-speed stream.[62] Direct measurement of the structure spacing from flow visualization images has been performed by several studies, with several results reported from the facility in which the Brown and Roshko experiments were performed.[1,8,63] Given a sufficiently large sample of structures, a reliable value for the mean spacing should be obtained from this method. Histograms of the structure spacing show significant variations around the mean value, with the study of Hernan and Jimenez yielding a mean value of $\bar{l}/(x - x_0) = 0.26$, and a most probable value of 0.23, for $s = 1$, $\lambda = 0.45$. Similarly, the most probable spacing from the Brown and Roshko experiment at $s = 7$, $\lambda = 0.45$ was 3% smaller than the mean value.

From the current simulations, it has been shown that both the visual thickness growth rate, $\delta_{viz}/(x - x_0)$, and the mean structure spacing, $\bar{l}/(x - x_0)$, are functions of both the density ratio, and the velocity ratio parameter. For both quantities, the functional relationship is $k\lambda/(1 + \Lambda\lambda)$, where the constant $k = k_\nu$ for the visual thickness growth rate, and $k = k_l$ for the mean structure spacing. Consequently, the ratio $\bar{l}/\delta_{viz}$ is found to be invariant across the range of density ratio and velocity ratios considered here, and attains a value of $\bar{l}/\delta_{viz} \approx 1.5$. The data of Brown and Roshko indicate that $\bar{l}/\delta_{viz} = 1.46$ for $s = 7$, $\lambda = 0.45$, and $\bar{l}/\delta_{viz} = 1.73$ based on a small sample for $s = 1/7$, $\lambda = 0.45$. The analysis of the Brown and Roshko cinefilm for $s = 1$, $\lambda = 0.45$ by Hernan and Jimenez yielded a value of $\bar{l}/\delta_{viz} = 1.605$. We therefore postulate that the scaling $\bar{l}/\delta_{viz}$ is invariant for the Brown–Roshko structure across s and λ, and attains a value in the region of 1.5–1.6, subject to measurement error. Regardless of the actual value of $\bar{l}/\delta_{viz}$, the dependency of the structure spacing on s and λ renders inappropriate the choice of structure spacing as a geometric progression to describe the entrainment ratio of the mixing layer.

The effect of the spanwise baroclinic vorticity generation on the variable density mixing layer simulated here is in agreement with the findings of Soteriou and Ghoniem,[31] who simulated the mixing layer confined to a two-dimensional computational domain. For the high-density ratio flow, negative spanwise vorticity is added to the spanwise structures on the high-speed side, and positive vorticity is added to them on the low-speed side. This situation is reversed for the low-density ratio flow. The simulation results reported here support the view that the baroclinic vorticity generation can be described by a dipole of vortices of opposite signs spanning the vortex structure, which induces a streamwise component of velocity and alters the convection speed of the flow.

Since the discovery of a stationary streamwise structure in the mixing layer, the ubiquity of the phenomenon for all initial conditions has been a contentious topic[65] and remains so at the time of writing.[38] Both the experimental studies[66] and numerical simulations[42] have shown that the stationary streamwise structure is absent for a mixing layer originating from a turbulent upstream boundary layer. For initially laminar conditions, experiments suggest that the structure may

be absent when elevated freestream turbulence is present,[65] and the structure is also absent in idealized numerical simulations of mixing layers perturbed by white noise fluctuations.[32,36–38,67] For initially laminar mixing layers originating from clean upstream conditions, experimental evidence across facilities shows broad agreement regarding the formation, and evolution, of the streamwise structure. Small non-uniformities in the upstream flow conditions produce residual streamwise vorticity within the laminar boundary layers which depart the splitter plate.[14,16,17,68] As this low-level vorticity propagates into the layer, it is amplified by the braid instability as the flow rolls up into K–H vortices, and the result is a single row of alternating-sign streamwise vortices along the span of the layer. The present simulation results demonstrate that the evolution of the stationary streamwise structure is universal for all s and λ, in that the maximum magnitude of streamwise vorticity attained is approximately 30% of the spanwise vorticity magnitude in the K–H roll-up, and that the streamwise vorticity decays in strength more rapidly than its spanwise counterpart. Where a single row of streamwise vortices exists in the layer, its spanwise wavelength scales with the local vorticity thickness, such that $\bar{l}_z/\delta_\omega \approx 1$. The simulation findings corroborate available experimental data[14,15,17] and extends the findings of a uniform density simulation study to the extreme values of the density ratio studied here.[35]

The current simulations demonstrate that the loss of coherence of the streamwise vortex structure is universal for all values of s and λ studied, with the loss of coherence occurring downstream of $P_x \approx 16$–22, in agreement with previous numerical simulations of the laboratory mixing layer.[35] For the uniform density flow conditions reported by Bell and Mehta,[15] ($\lambda = 0.25$, $\theta_i = 0.53$ mm), they observed that the streamwise vortices became "ragged" in appearance beyond $x = 1.08$ m, which corresponds to a pairing parameter value $P_x \approx 17$. Evidence for the loss of coherence in the streamwise vortex structure occurring in the variable density laboratory flow can be found in Figs. 5 and 6 of Bernal and Roshko[14]— qualitative estimates of the momentum thickness of the high-speed stream can be determined from the initial K–H vortex spacing in the layer, yielding $\theta_i \approx 0.1$ mm. Where the streamwise structure loses its coherence in the time-averaged visualization of their Fig. 6 coincides approximately to the position where the third generation of interactions between spanwise structures has been completed, i.e., $P_x > 16$. Note that these estimates are based on a single-snapshot visualization, but we are inclined to consider the obtained qualitative values as indicative of the evolution of the streamwise structure evolution in the laboratory flow. We postulate that the loss of coherence of the stationary streamwise structure is a universal feature of the laboratory mixing layer originating from clean upstream conditions, and the findings imply that the Brown–Roshko structure is still evolving at non-dimensional streamwise distances where the mixing layer is considered to be in a fully-developed, self-similar state. Further evidence for the continuing evolution of the vortex structure can be found in scalar concentration probability density function measurements, which display a shift from a non-marching form to a tilted form at $P_x \approx 16$–22,[5] which has been linked to the loss of coherence of the streamwise structure.[35]

We note that the streamwise component of baroclinic vorticity generation has an influence on the mean streamwise structure, with the addition of positive and negative streamwise vorticity giving the mean streamwise structure a corrugated appearance along the span of the layer. The statistical properties of the streamwise structures presented here, however, indicate that the influence of baroclinic vorticity generation on the streamwise vortex structure is relatively minor.

Evidence from experimental studies,[11,69,70] and two-dimensional numerical simulations,[31] indicates that the entrainment ratio between the freestreams, and the pattern of mixing within the layer, is also markedly influenced by the density ratio between the freestreams. In this article, we have focused on the effects of the density ratio on the large-scale structure, and on the dynamics of the flow. The topics of mixing and entrainment, while intertwined with the dynamics of the large-scale structures in the mixing layer, warrant extensive discussion in their own right, and results from the current simulations concerning the entrainment and mixing of a conserved scalar will be discussed in a future article.

VIII. CONCLUSIONS

Large eddy simulation has been used to investigate the effects of density ratio on the low-speed, incompressible plane turbulent mixing layer, originating from laminar upstream conditions which are representative of laboratory flows. It has been shown that, at non-uniform density conditions, the mean flow statistics are biased toward the low-density stream, and that for a given density ratio the peak magnitudes of the turbulence statistics are a function of the velocity ratio parameter, in agreement with previous temporal simulation findings. The visual growth rate of the layer is a function of both density ratio and velocity ratio parameter in agreement with experimental findings, and the rate of growth of the layer matches that observed in experiments. It has been found that the spacing of the large-scale, spanwise orientated turbulent vortex structures is a function of both the velocity ratio parameter between the freestreams, and the density ratio parameter. When scaled by the local visual thickness of the layer, the normalized structure spacing in the incompressible variable density mixing layer, $\bar{l}/\delta_{viz}$ attains a value of approximately 1.5, for all values of the density ratio. The streamwise structure evolves to attain a spanwise wavelength that scales with the local vorticity thickness, and the structures lose their coherence downstream of approximately the third generation of interactions between primary spanwise vortices, independent of the density ratio and velocity ratio parameter. The current findings provide further evidence that the Brown–Roshko structure continues to evolve at streamwise distances where the flow is typically considered to be fully developed, for the particular set of clean laminar inflow conditions considered here.

The present findings have important implications for the development of new models to describe the growth and entrainment of the low-speed mixing layer, and further research is required in order to produce improved models to describe these phenomenon. A comprehensive discussion of the mixing and entrainment in the variable density mixing layer will appear in a future publication.

It is important to note that the conclusions drawn from the present findings are valid for the range of density ratio covered in this study, and it is not clear if the scaling laws for the mixing layer growth rate, and the normalized structure spacings, will persist to more extreme values of the density ratio. More research is required to confirm the trends observed here over a wider range of the density ratio.

ACKNOWLEDGMENTS

This research used ALICE, the University of Leicester High Performance Computing facility. Further research simulations were performed using TAURUS, the Aston University High Performance Computing facility.

AUTHOR DECLARATIONS

Conflict of Interest

The authors have no conflicts to disclose.

Author Contributions

W. A. McMullan: Conceptualization (lead); Data curation (lead); Formal analysis (equal); Investigation (lead); Methodology (equal); Supervision (equal); Validation (equal); Writing – original draft (equal); Writing – review & editing (equal). **J. X. Huang:** Formal analysis (equal); Investigation (equal); Visualization (equal); Writing – review & editing (equal). **S. N. Hug:** Formal analysis (equal); Investigation (equal); Visualization (equal); Writing – review & editing (equal). **J. Mifsud:** Formal analysis (equal); Validation (equal); Writing – original draft (equal); Writing – review & editing (equal). **S. J. Garrett:** Supervision (equal); Writing – review & editing (equal).

DATA AVAILABILITY

The data that support the findings of this study are available from the corresponding author upon reasonable request.

APPENDIX: EFFECTS OF VARIABLE VISCOSITY

The simulations presented in the main body of this article assume a constant value of the fluid dynamic viscosity, μ. A more accurate means to model the dynamic viscosity of the dissimilar gases following the procedure of Wilke,[71] such that for the high-density ratio simulations the dynamics viscosity is computed through

$$\mu = \frac{1.952 \times 10^{-5}\zeta}{\zeta + 2.419(1-\zeta)} + \frac{1.813 \times 10^{-5}(1-\zeta)}{0.3105\zeta + (1-\zeta)}, \tag{A1}$$

and for the low-density ratio simulations, the dynamic viscosity is computed using the expression

$$\mu = \frac{1.813 \times 10^{-5}\zeta}{\zeta + 0.3105(1-\zeta)} + \frac{1.952 \times 10^{-5}(1-\zeta)}{2.419\zeta + (1-\zeta)}, \tag{A2}$$

assuming that the gases have a temperature of 293 K. In this Appendix, cases 3 ($s = 0.138$, $\lambda = 0.66$) and 9 ($s = 7.23$, $\lambda = 0.66$) are re-run with the dynamic viscosity computed through Eqs. (A1) and (A2), respectively. All other simulation parameters are held constant with respect to those presented above. The simulations with variable dynamic viscosity are denoted 3v and 9v, for clarity.

Contour maps of the instantaneous dynamic viscosity in the flow, normalized by the dynamic viscosity of air, are shown in Fig. 29. It can be observed that the dynamic viscosity increases where mixing between the dissimilar gases occurs within the layer.

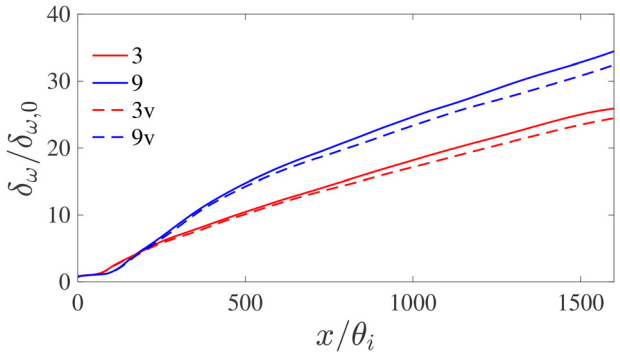

FIG. 30. Vorticity thickness distribution in cases 3, 9, 3v, and 9v.

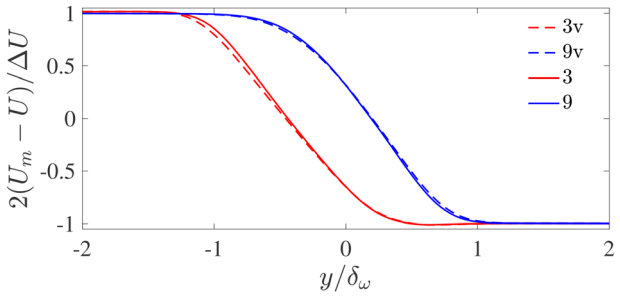

FIG. 31. Mean streamwise velocity profiles, extracted from a downstream distance of $x/\theta_i = 1000$.

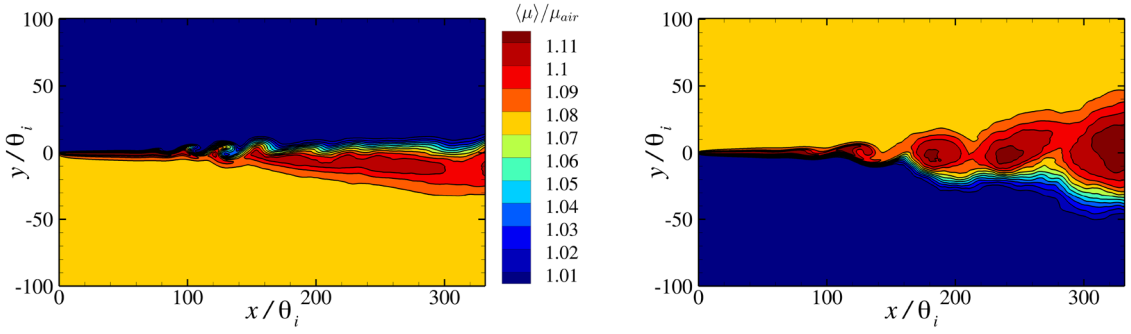

(a)Case 3v. (b)Case 9v.

FIG. 29. Contour maps of the spanwise-averaged molecular viscosity, captured at an arbitrary instant in time.

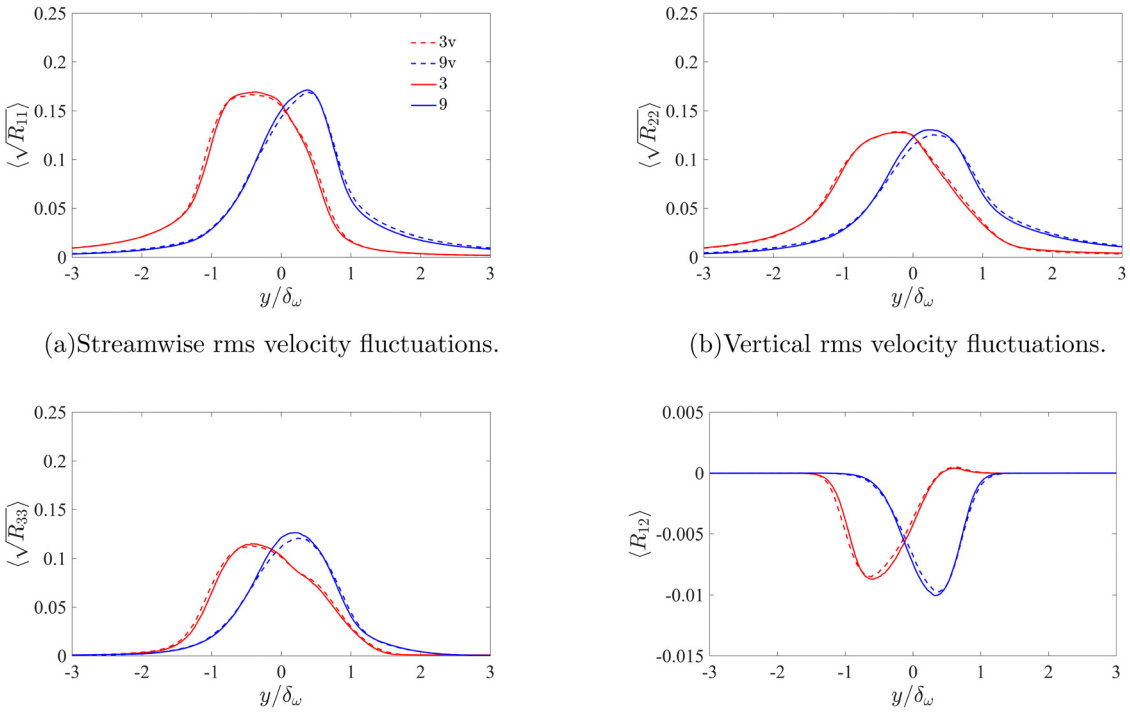

(a)Streamwise rms velocity fluctuations.

(b)Vertical rms velocity fluctuations.

(c)Spanwise rms velocity fluctuations.

(d)Primary Reynolds shear stress.

FIG. 32. Turbulence statistics extracted from the simulations at $x/\theta_i = 1000$.

The vorticity thickness distributions of the four simulations considered here are shown in Fig. 30. When variable dynamic viscosity is incorporated into the simulations, the predicted vorticity thickness in the self-similar region is 5% smaller than the counterpart simulation with constant dynamic viscosity, for both values of the density ratio. The gradient of the linear slope of the vorticity thickness is, however, largely unaffected, and the slight thinning of the layer merely corresponds to a shift in the virtual origin of the flow in cases 3v and 9v, when compared to cases 3 and 9, respectively. The structure spacing constant, k_l, and the visual thickness growth rate constant, k_v are identical for both the uniform dynamic viscosity calculations, and the variable dynamic viscosity counterparts.

The normalized mean streamwise velocity extracted from $x/\theta_i = 1000$ is shown in Fig. 31. The agreement between the simulations for a given density ratio is extremely good, and shift of the velocity profile toward the low-density stream is maintained. The normalized turbulence statistics extracted from the same downstream location are shown in Fig. 32. All four statistical quantities display minimal variations in the computed turbulent statistics for a given density ratio, with the largest discrepancy being in the prediction of $\sqrt{R_{33}}$ for case 9v. The variations between the simulations, however, are well within the $\pm 0.5\%$ scatter in the fluctuations reported in the uniform density reference experiment.

The results presented here show that the effect of variable dynamic viscosity on the simulated variable density mixing layer is negligible, for the current simulation setup. We conclude that there is sufficient justification to perform the simulations with a constant dynamic viscosity, without any significant loss in accuracy of the simulation predictions.

REFERENCES

[1]G. L. Brown and A. Roshko, "On density effects and large structure in turbulent mixing layers," J. Fluid Mech. **64**, 775–816 (1974).
[2]P. E. Dimotakis, "The mixing transition in turbulent flows," J. Fluid Mech. **409**, 69–98 (2000).
[3]P. E. Dimotakis and G. L. Brown, "The mixing layer at high Reynolds number: Large-structure dynamics and entrainment," J. Fluid Mech. **78**, 535–560 (1976).
[4]M. Koochesfahani, P. E. Dimotakis, C. J. Catherasoo, M. Gharib, and D. B. Lang, "Two-point LDV measurements in a plane mixing layer," AIAA J. **17**, 1347–1351 (1979).
[5]P. S. Karasso and M. G. Mungal, "Scalar mixing and reaction in plane liquid shear layers," J. Fluid Mech. **323**, 23–63 (1996).
[6]A. D'Ovidio and C. M. Coats, "Organized large structure in the post-transition mixing layer. Part 1. Experimental evidence," J. Fluid Mech. **737**, 466–498 (2013).
[7]R. Breidenthal, "Structure in turbulent mixing layers and wakes using a chemical reaction," J. Fluid Mech. **109**, 1–24 (1981).
[8]M. A. Hernan and J. Jimenez, "Computer analysis of a high-speed film of the plane turbulent mixing layer," J. Fluid Mech. **119**, 323–345 (1982).
[9]M. G. Mungal and P. E. Dimotakis, "Mixing and combustion with low heat release in a turbulent shear layer," J. Fluid Mech. **148**, 349–382 (1984).
[10]J. C. Hermanson and P. E. Dimotakis, "Effects of heat release in a turbulent, reacting shear layer," J. Fluid Mech. **199**, 333–375 (1989).

[11]J. H. Konrad, "An experimental investigation of mixing in two-dimensional turbulent shear flows with applications to diffusion-limited chemical reactions," Ph.D. thesis (Caltech, 1976).
[12]P. E. Dimotakis, "Two-dimensional shear-layer entrainment," AIAA J. **24**, 1791–1796 (1986).
[13]A. R. Kerstein, "Growth-rate prediction for low-speed variable-density spatially developing turbulent planar shear layers: Status and prospects," J. Fluids Eng. **145**, 104501 (2023).
[14]L. P. Bernal and A. Roshko, "Streamwise vortex structure in plane mixing layers," J. Fluid Mech. **170**, 499–525 (1986).
[15]J. H. Bell and R. D. Mehta, "Measurements of the streamwise vortical structures in a plane mixing layer," J. Fluid Mech. **239**, 213–248 (1992).
[16]L.-S. Huang and C.-M. Ho, "Small-scale transition in a plane mixing layer," J. Fluid Mech. **210**, 475–500 (1990).
[17]J. Jimenez, "A spanwise structure in the plane shear layer," J. Fluid Mech. **132**, 319–336 (1983).
[18]J. C. Lasheras, J. S. Cho, and T. Maxworthy, "On the origin and evolution of streamwise vortical structures in a plane, free shear layer," J. Fluid Mech. **172**, 231–258 (1986).
[19]K. C. Wiecek and R. D. Mehta, "Effects of velocity ratio on mixing layer three-dimensionality," Exp. Therm. Fluid Sci. **16**, 165–176 (1998).
[20]C. Pantano and S. Sarkar, "A study of compressibility effects in the high-speed turbulent shear layer using direct simulation," J. Fluid Mech. **451**, 329–371 (2002).
[21]A. Almagro, M. García-Villalba, and O. Flores, "A numerical study of a variable-density low-speed turbulent mixing layer," J. Fluid Mech. **830**, 569–601 (2017).
[22]J. R. Baltzer and D. Livescu, "Low-speed turbulent shear-driven mixing layers with large thermal and compositional density variations," in *Modeling and Simulation of Turbulent Mixing and Reaction: For Power, Energy and Flight*, edited by D. Livescu, A. G. Nouri, F. Battaglia, and P. Givi (Springer Singapore, Singapore, 2020), pp. 1–23.
[23]J. R. Baltzer and D. Livescu, "Variable-density effects in incompressible non-buoyant shear-driven turbulent mixing layers," J. Fluid Mech. **900**, A16 (2020).
[24]K. Arora, K. Chakravarthy, and D. Chakraborty, "Large eddy simulation of supersonic, compressible, turbulent mixing layers," Aerosp. Sci. Technol. **86**, 592–598 (2019).
[25]C. Le Ribault, "Large eddy simulation of passive scalar in compressible mixing layers," Int. J. Heat Mass Transfer **51**, 3514–3524 (2008).
[26]N. D. Sandham and R. D. Sandberg, "Direct numerical simulation of the early development of a turbulent mixing layer downstream of a splitter plate," J. Turbul. **10**, N1 (2009).
[27]D. Zhang, J. Tan, and X. Yao, "Direct numerical simulation of spatially developing highly compressible mixing layer: Structural evolution and turbulent statistics," Phys. Fluids **31**, 036102 (2019).
[28]Q. Zhou, F. He, and M. Y. Shen, "Direct numerical simulation of a spatially developing compressible plane mixing layer: Flow structures and mean flow properties," J. Fluid Mech. **711**, 437–468 (2012).
[29]M. R. Mankbadi, J. R. DeBonis, and N. J. Georgiadis, "Large-eddy simulation of a compressible mixing layer and the significance of inflow turbulence," in *55th AIAA Aerospace Sciences Meeting* (AIAA, 2017).
[30]G. Matheou, A. M. Bonanos, C. Pantano, and P. E. Dimotakis, "Large-eddy simulation of mixing in a recirculating shear flow," J. Fluid Mech. **646**, 375–414 (2010).
[31]M. C. Soteriou and A. F. Ghoniem, "Effects of the free-stream density ratio on free and forced spatially developing shear layers," Phys. Fluids **7**, 2036–2051 (1995).
[32]W. A. McMullan and S. J. Garrett, "Initial condition effects on large scale structure in numerical simulations of plane mixing layers," Phys. Fluids **28**, 015111 (2016).
[33]W. McMullan, "Spanwise domain effects on streamwise vortices in the plane turbulent mixing layer," Eur. J. Mech.-B **67**, 385–396 (2018).
[34]S. Hug and W. McMullan, "The influence of velocity ratio on the evolution of streamwise vortices in the simulated plane mixing layer," Eur. J. Mech.-B **76**, 166–177 (2019).
[35]S. N. Hug, W. A. McMullan, J. Mifsud, and S. J. Garrett, "Resolved scalar mixing in large eddy simulations of the laboratory mixing layer," Phys. Fluids **37**, 045148 (2025).
[36]W. A. McMullan, S. Gao, and C. M. Coats, "Organised large structure in the post-transition mixing layer. Part 2. Large-eddy simulation," J. Fluid Mech. **762**, 302–343 (2015).
[37]J. X. Huang and W. A. McMullan, "Mixing and combustion at low heat release in large eddy simulations of a reacting shear layer," Theor. Comput. Fluid Dyn. **35**, 553–580 (2021).
[38]C. Coats, "Organised large structure in the post-transition mixing layer. Part 3. Dynamics of the spatial growth," J. Fluid Mech. **997**, A63 (2024).
[39]J. X. Huang, S. N. Hug, and W. A. McMullan, "Large eddy simulation of the variable density mixing layer," Fluid Dyn. Res. **53**, 015507 (2021).
[40]C. G. Koop and F. K. Browand, "Instability and turbulence in a stratified fluid with shear," J. Fluid Mech. **93**, 135–159 (1979).
[41]F. Nicoud and F. Ducros, "Subgrid-scale stress modelling based on the square of the velocity gradient tensor," Flow, Turbul. Combust. **62**, 183–200 (1999).
[42]W. A. McMullan, J. Mifsud, and M. Angelino, "The growth of the initially turbulent mixing layer: A large eddy simulation study," Phys. Fluids **36**, 115194 (2024).
[43]W. A. McMullan, S. Gao, and C. M. Coats, "A comparative study of inflow conditions for two- and three-dimensional spatially developing mixing layers using large eddy simulation," Int. J. Numer. Methods Fluids **55**, 589–610 (2007).
[44]W. McMullan, S. Gao, and C. Coats, "The effect of inflow conditions on the transition to turbulence in large eddy simulations of spatially developing mixing layers," Int. J. Heat Fluid Flow **30**, 1054–1066 (2009).
[45]F. Xiao, M. Dianat, and J. J. McGuirk, "An LES turbulent inflow generator using a recycling and rescaling method," Flow, Turbul. Combust. **98**, 663–695 (2017).
[46]P. Wang and J. McGuirk, "Validation of a large eddy simulation methodology for accelerated nozzle flows," Aeronaut. J. **124**, 1070–1098 (2020).
[47]F. Xiao, M. Dianat, and J. McGuirk, "LES of turbulent liquid jet primary breakup in turbulent coaxial air flow," Int. J. Multiphase Flow **60**, 103–118 (2014).
[48]W. McMullan and M. Angelino, "The effect of tree planting on traffic pollutant dispersion in an urban street canyon using large eddy simulation with a recycling and rescaling inflow generation method," J. Wind Eng. Ind. Aerodyn. **221**, 104877 (2022).
[49]J. L. Brown, "Heterogeneous turbulent mixing layer investigations utilizing a 2-D 2-color laser doppler anemometer and concentration probe," Ph.D. thesis (University of Missouri, Columbia, 1978).
[50]B. Dziomba and H. E. Fiedler, "Effect of initial conditions on two-dimensional free shear layers," J. Fluid Mech. **152**, 419–442 (1985).
[51]W. McMullan, "Spanwise domain effects on the evolution of the plane turbulent mixing layer," Int. J. Comput. Fluid Dyn. **29**, 333–345 (2015).
[52]J. H. Bell, M. W. Plesniak, and R. D. Mehta, "Spanwise averaging of plane mixing layer properties," AIAA J. **30**, 835–837 (1992).
[53]F. K. Browand and B. O. Latigo, "Growth of the two-dimensional mixing layer from a turbulent and nonturbulent boundary layer," Phys. Fluids **22**, 1011–1019 (1979).
[54]D. Yoder, J. DeBonis, and N. Georgiadis, "Modeling of turbulent free shear flows," Comput. Fluids **117**, 212–232 (2015).
[55]A. Hadjadj and A. Kudryavtsev, "Computation and flow visualization in high-speed aerodynamics," J. Turbul. **6**, N16 (2005).
[56]F. K. Browand and T. R. Troutt, "A note on spanwise structure in the two-dimensional mixing layer," J. Fluid Mech. **97**, 771–781 (1980).
[57]F. K. Browand and T. R. Troutt, "The turbulent mixing layer: Geometry of large vortices," J. Fluid Mech. **158**, 489–509 (1985).
[58]L. P. Bernal, "The statistics of the organized vortical structure in turbulent mixing layers," Phys. Fluids **31**, 2533–2543 (1988).
[59]J. Jimenez, M. Cogollos, and L. P. Bernal, "A perspective view of the plane mixing layer," J. Fluid Mech. **152**, 125–143 (1985).
[60]G. L. Brown and A. Roshko, "Turbulent shear layers and wakes," J. Turbul. **13**, N51 (2012).
[61]P. Bradshaw, "The effect of initial conditions on the development of a free shear layer," J. Fluid Mech. **26**, 225–236 (1966).
[62]B. W. Spencer and B. G. Jones, "Statistical investigation of pressure and velocity fields in the turbulent two-stream mixing layer," in *4th Fluid and Plasma Dynamics Conference* (AIAA, 1971). https://arc.aiaa.org/doi/pdf/10.2514/6.1971-613.

[63]L. Bernal, "The coherent structure of turbulent mixing layers," Ph.D. thesis (Caltech, 1981).
[64]M. M. Koochesfahani and P. E. Dimotakis, "Mixing and chemical reactions in a turbulent liquid mixing layer," J. Fluid Mech. **170**, 83–112 (1986).
[65]C. Chandrsuda, R. D. Mehta, A. D. Weir, and P. Bradshaw, "Effect of free-stream turbulence on large structure in turbulent mixing layers," J. Fluid Mech. **85**, 693–704 (1978).
[66]J. H. Bell and R. D. Mehta, "Development of a two-stream mixing layer from tripped and untripped boundary layers," AIAA J. **28**, 2034–2042 (1990).
[67]A. Attili and F. Bisetti, "Statistics and scaling of turbulence in a spatially developing mixing layer at $Re_\lambda = 250$," Phys. Fluids **24**, 035109 (2012).
[68]J. C. Lasheras and H. Choi, "Three-dimensional instability of a plane free shear layer: An experimental study of the formation and evolution of streamwise vortices," J. Fluid Mech. **189**, 53–86 (1988).
[69]G. L. Brown, "The entrainment and large structure in turbulent mixing layers," in *5th Australasian Conference on Hydraulics and Fluid Mechanics* (University of Canterbury, 1975), Vol. 1, pp. 352–359.
[70]C. Frieler, "Mixing and reaction in the subsonic two-dimensional turbulent free shear layer," Ph.D. thesis (Caltech, 1992).
[71]C. R. Wilke, "A viscosity equation for gas mixtures," J. Chem. Phys. **18**, 517–519 (1950).